Characterization of the proton beam line in the experimental room of HollandPTC

Atia Ibrahimi

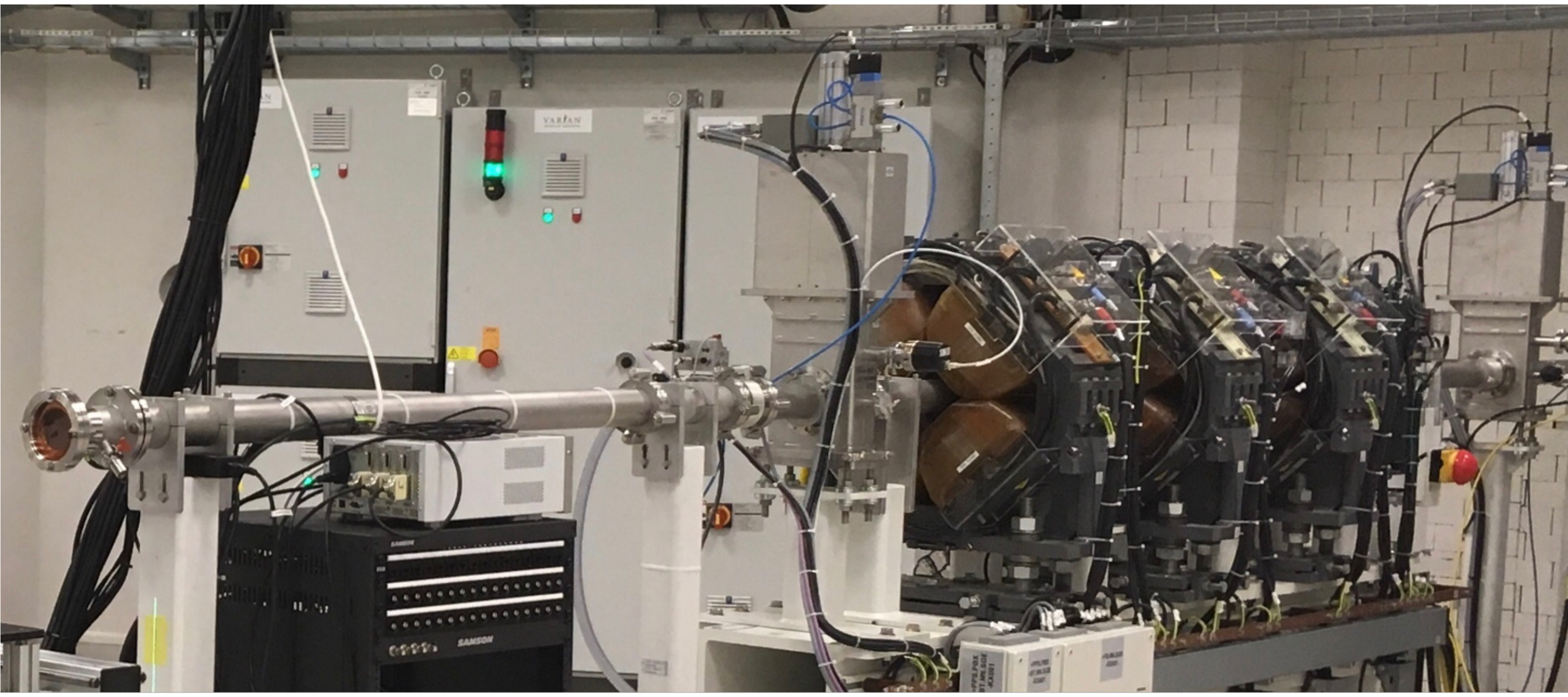

Characterization of the proton beam line in the experimental room of HollandPTC

by

Atia Ibrahimi

to obtain the degree of Master of Science in Biomedical Engineering
at the Delft University of Technology,
to be defended publicly on Tuesday December 1, 2020 at 10:00 AM.

Student number:	4221796	
Committee:	Dr. Ir. Danny Lathouwers	TU Delft
	Dr. Anna Louise Smith	TU Delft
	Dr. Steven Parnell	TU Delft
	Dr. Marta Rovituso	HollandPTC

Contents

Abstract

As protons have a localized depth-dose distribution, proton therapy nowadays is a form of radiotherapy that is being implemented for part of the cancer patients. Compared to photon therapy it allows more precise targeting of tumours and sparing of surrounding healthy tissue. Besides patient treatment, research on proton therapy topics is being done to gain more knowledge on and keep improving the technique.

Since the 1950s almost 100 proton therapy facilities are operating clinically worldwide. One of those facilities is HollandPTC, a proton therapy center located in Delft, The Netherlands. The ProBeam Varian cyclotron serves two treatment gantries, an eye treatment room, and a research experimental room. The experimental room is dedicated to research topics in the proton therapy field and is equipped with a fixed horizontal beam line that can be used for physics experiments and also for radiobiological experiments. In order to perform those types of research the beam needs to be fully characterized in terms of dose, shape, size and energy, this is the purpose of this work. The second goal was to commence with a setup for creating homogeneous fields by means of passive scattering and determine the optimal distances required between the elements of the setup.

The single pencil beam characterization has been done by performing a large variety of experiments, making use of setups with different types of detectors. The experiments include beam spot, beam envelope, beam current, and depth-dose distribution measurements, and have been performed for nominal beam energies between 70 and 240 MeV. For the passively scattered field a dual ring setup has been implemented. Spread-out Bragg peaks have been created with a ridge filter. An energy of 150 MeV was used, as the scattering elements have been designed for this energy specifically.

The single pencil beam characterization resulted in beam spot sizes at the isocenter varying from 3.54 mm for 240 MeV, up to 5.47 mm for 70 MeV, with an asymmetry of 1.7% at most. The beam envelope measurements showed that the beam spot size just after the exit window is 2-3 mm and diverges up to 12 mm at 2 m from the exit window. The beam current measurements gave the transmission efficiency of the system, ranging from 0.04% for a 70 MeV beam up to 5.6% for 240 MeV, increasing exponentially. The depth-dose measurements provided the difference between the nominal beam energy and the beam energy at the isocenter. The difference becomes smaller as the nominal beam energy increases and is 2.4% for a 70 MeV nominal beam and 0.3% for a 230 MeV nominal beam. With the dual ring setup fields of up to 25 cm in diameter have been formed with a uniformity of at least 97%. The ridge filter created a spread-out Bragg peak of 2.8 cm with a uniformity of 98% and also gave good results for other beam energies (100-200 MeV).

It can be concluded that the goals of the project have been reached as the beam has been characterized in terms of shape, current, and energy. Also some preliminary work for the passive field has been accomplished. The work on the dual ring setup can be further expanded by placing the ridge filter and a collimator in the setup, after which the field can be characterized in terms of dose. The results obtained from the single pencil beam characterization allowed for the first physics experiments to start at the experimental room of HollandPTC during the last year.

Preface

This is the report for my master thesis project, to finalize the Master of Biomedical Engineering at Delft University of Technology (TU Delft). The project has been completed within the Medical Physics & Technology research group of the Radiation Science & Technology department of the Applied Sciences faculty of TU Delft, and the Research & Development department of Holland Proton Therapy Centre (HollandPTC).

First of all I would like to thank everyone from both departments for providing such an enjoyable working environment during the past months. During the project I have received the support of my two supervisors Danny Lathouwers and Marta Rovituso. I would like to thank Danny for providing valuable feedback and keeping me critical of my work during our progress meetings, and for making sure I was doing okay during the period that I had to work from home out of necessity. To Marta I am very grateful for providing me with a fantastic project and trusting me with this enormous responsibility. Also thank you for teaching Henar and me to take a small dance break when a difficult experiment is starting to work.

Henar, thank you for making my time at HollandPTC extra awesome. It has been great to spend my days with a dear friend. I had so much fun working together during all those months, and at the same time I could always count on you when I needed help.

I want to thank my Zumba family for helping me to clear my head when I needed it, and at the same time being so supportive when I could not be there countless times. Especially to Samantha, Yadira, and Natalia: Thank you for being such good friends, even when we didn't see each other for months sometimes.

Finally I want to thank my family for being so supportive, believing in me, and being such good role models. My Mom and Dad who have been taking great care of me and have been so involved. Khatera, Obayd, Ahmad, and Roya I knew I could always count on you and ask for valuable advice. Sander, I could not have wished for a better partner. You have always had my back, helped me when I needed it without any complaints, and made my life wonderful.

Thank you all very much!

Atia Ibrahimi
Delft, November 2020

Introduction

Radiation therapy

Every year millions of cancer cases are discovered worldwide. It has been estimated that in 2018 there have been 18.1 million new cases [9]. For the same year it has been estimated by the World Health Organization that cancer has been responsible for 9.6 million deaths, making it the second leading cause of death [48]. More than half of the cancer patients with malignant tumours get treated with radiation therapy [37], either on its own or alongside other treatments such as surgery and chemotherapy.

Radiation therapy kills cancerous cells by damaging the DNA directly or indirectly. In the case of direct DNA damage the ionizing radiation will deposit energy to the DNA. Indirect DNA damage happens when the ionizing radiation interacts with a water molecule and creates a free radical, which then damages the DNA. The three major types of DNA damage are base and sugar damage, single strand breaks (SSBs), and double strand breaks (DSBs) [18]. A schematic of the three types is shown in figure 1. DNA damage can be repaired, but the repair of DSBs is difficult. Even when DSBs are repaired, it can happen that the broken ends are rejoined incorrectly, leading to cell death. The goal of radiation therapy is to cause damage to cancerous tissue and at the same time spare as much healthy tissue as possible.

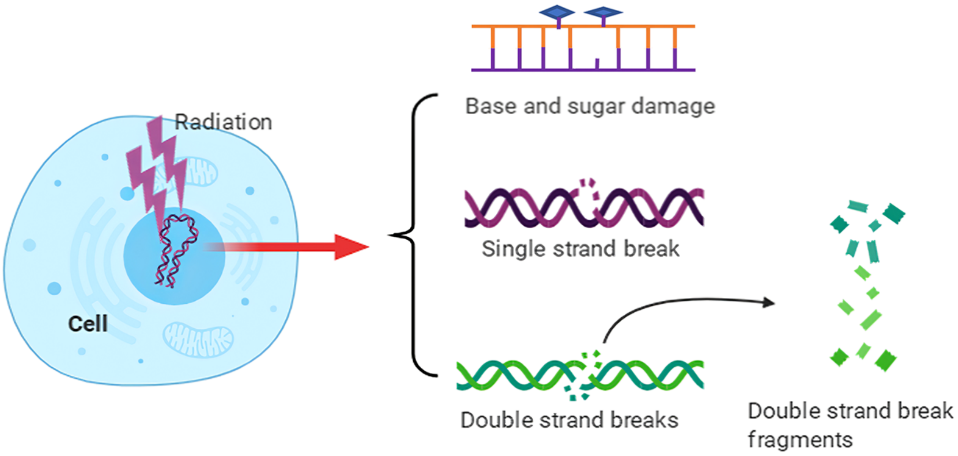

Figure 1: DNA damage induced by ionizing radiation, showing base and sugar damage, single strand breaks, and double strand breaks. Figure taken from Huang et al. [18].

Proton therapy

The most common choice for radiation therapy is photon-based external beam therapy [15]. The first documented patient treatment with photon therapy was in 1896 [1]. Nowadays a small part of the patients however is treated with charged particle therapy, which has a favourable depth-dose distribution. Figure 2 shows the depth-dose distribution for photons, protons, and carbon ions. For the latter two the distribution is also known as the Bragg peak due to the characteristic shape. From the figure it can be seen that the dose deposition is more localized for protons and carbon ions compared to photons. The localized dose deposition allows more precise targeting of tumours and sparing of surrounding healthy tissue. Applying heavy charged particles to radiotherapy was considered first in 1946 by Robert R. Wilson [49], when he investigated the application of protons to treat tumours that are located deep within healthy tissue. In the article Wilson also discusses a rotating wheel of variable thicknesses, which is known as a range modulator, placed between the source and the patient to create a spread-out Bragg peak for treatment of large tumours.

The first patients were treated with protons at Lawrence Berkeley Laboratory in 1954 [29, 37], almost 50 years later than the first patients treated with photons. This is why besides clinical practice, a lot of research is being done in the field of proton therapy to get a better understanding and keep improving the technique. Nowadays almost 100 proton therapy facilities are operating clinically worldwide [35]. Three of them are located in The Netherlands: UMC PTC in Groningen, ZON PTC in Maastricht, and HollandPTC in Delft.

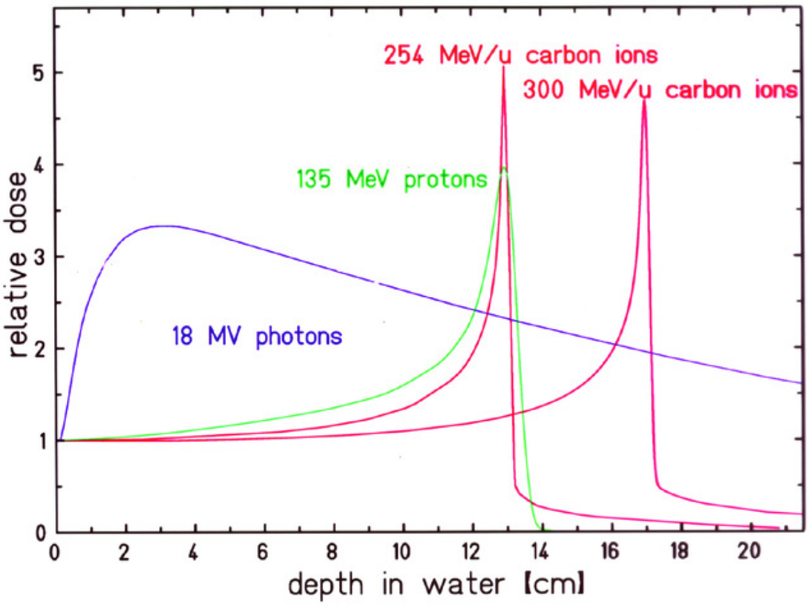

Figure 2: Depth-dose curves in water for photons, protons, and carbon ions. Figure taken from Durante et al. [12].

HollandPTC

HollandPTC (HPTC) is a consortium founded by Erasmus Medical Center (Erasmus MC), Leiden University Medical Center (LUMC), and Delft University of Technology (TU Delft), which focuses not only on the clinical aspects, but also on a large variety of research topics in the proton therapy field. In this respect, radiobiology research, clinical trials, advanced technology, and predictive model research are carried out at HPTC. The ProBeam Varian cyclotron at HPTC serves two treatment gantries, an eye treatment room, and a research experimental room. An overview of the center is shown in figure 3. The consortium partners are the main users of the HPTC facility, which can be exploited under different aspects, from the usage of the imaging setup (CT, PET-CT, MRI) to the experimental area which includes biology, physics, and chemistry laboratories. The experimental room is equipped with a fixed horizontal beam line, which can be used for physics experiments as they often require a narrow spot. Radiobiological experiments on the other hand require a broad homogeneous field to irradiate cell samples and tumours in animals.

Goals

In an experimental setup the characteristics of the beam hitting the target are crucial. Beam characteristics are also useful when designing and preparing an experiment. Information can be obtained on the beam profile at the target, which gives the lateral spread and the beam spot size. Additionally the beam current allows to determine how many protons arrive at the target (in a certain time window), or can be used to obtain the dose rate. Finally the beam energy at the target is significant for the depth-dose distribution and range. The proton beams in the treatment gantries and eye treatment room at HPTC had been characterized already, whereas the proton beam in the experimental room still needed to be characterized before being used, resulting in the first and main goal of this thesis:

- Characterization of the fixed single pencil beam in the experimental room in terms of shape, current, and energy.

The characterization will be executed for nominal beam energies varying from the lowest energy of 70 MeV up to the highest beam energy of 240 MeV. As radiobiological experiments require a broad homogeneous field, once the single pencil beam is characterized, the broad field can be created with a passive scattering technique and then characterized in terms of dose. The second goal of the project is:

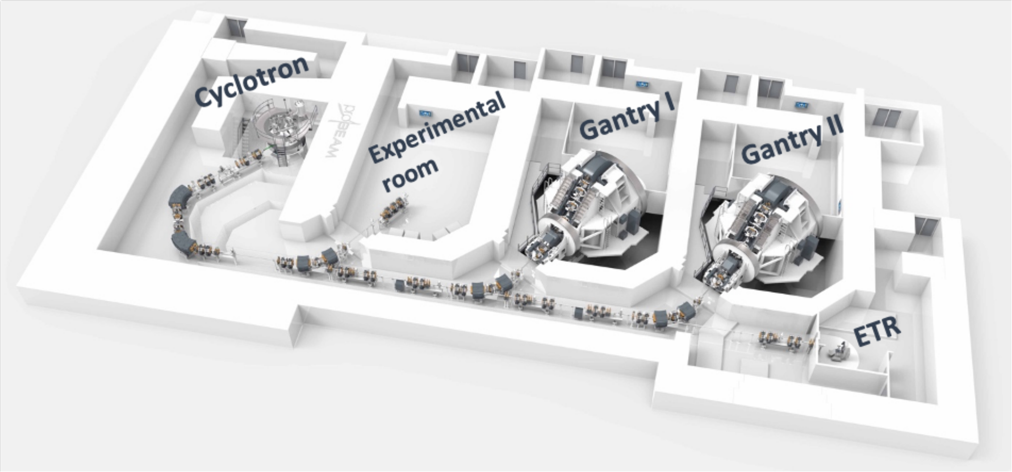

Figure 3: Overview of HollandPTC showing the cyclotron serving the experimental room, two treatment gantries, and the eye treatment room (ETR). Courtesy of Varian.

- Commence with creating a broad uniform field and experimentally determine the optimal distances required between the elements of the passive scattering setup.

Further optimization and characterization of the passively scattered field are out of the scope of this project and have been performed in another thesis project by M.D.H. Rituerto Prieto [34]

Structure

This report consists of five chapters. In the first chapter the research background on proton interactions and cyclotron systems are given to gain insight on which aspects influence the beam characteristics. Furthermore some passive scattering techniques will be explained to gain knowledge on how a passive scattering setup can be used to create a big field out of a single pencil beam. In the next chapter a literature study is presented, which focuses on methods of beam characterization. The purpose of the literature study was to find how beam characterization usually is performed and to then be able to choose appropriate methods for this thesis. In chapter three the materials for the proton beam characterization are described together with an experimental setup for every type of experiment that has been performed. Additionally a description is given on how the data of the experiments have been processed. Chapter four presents and discusses the results that have been obtained, followed by the conclusions and future prospects in chapter five.

1

Research Background

In this chapter the theory behind aspects that are of importance for the beam characteristics are explained. The focus is mainly on interactions of protons with matter and the operation principle of a cyclotron system. Together this shows where proton beam characteristics originate from. Finally, some explanations are given on passive scattering techniques, which are of importance when working with a single pencil beam with a fixed beam line without nozzle, as is the case in the HollandPTC research room.

1.1. Proton beam interactions

Protons interact with matter in three ways, namely scattering, nuclear interactions, and stopping. These interactions will affect a proton beam in terms of shape, fluence, and energy [29]. The interactions and their effects on the characteristics are explained in the sections below.

1.1.1. Lateral beam spread: multiple Coulomb scattering

Scattering

Scattering is an electromagnetic interaction which occurs when a proton is deflected by an atomic nucleus. The deflection caused by one nucleus usually will be very small. Observable angular spread of a proton beam interacting with matter will be caused by many deflections combined [29]. This is why scattering is also called multiple Coulomb scattering (MCS).

The beam profile is the spatial distribution of the protons in the xy-plane perpendicular to the proton beam. The spatial distribution gets its shape mostly due to MCS in matter and it follows a nearly Gaussian distribution. The distribution is not completely Gaussian due to single scattering at larger angles, which occurs rarely, but does have a contribution to the profile. The result is a distribution with a Gaussian core from the MCS, where about 98% of the protons will be, and single scattering tails. Scattering angles are usually limited to a few degrees (e.g. 160 MeV protons traversing 1 g/cm^2 of water), but they can reach up to sixteen degrees (e.g. 160 MeV protons traversing 1 g/cm^2 of lead) [5]. Materials with a higher atomic number (Z) will scatter the beam more strongly and protons with lower energies have bigger scattering angles. Figure 1.1 shows a proton beam passing a slab of material, traversing a distance L to a measuring plane (MP). At the MP the distribution of the particles is shown to be nearly Gaussian.

Several theories exist that predict the exact distribution of the MCS together with the width of the distribution as a function of proton energy, scattering material, and the thickness of the material. One of them is Molière's Theory [24][25], which predicts this distribution the most accurate. The theory however is algebraically complicated, whereas Highland's formula [17] is easier to evaluate and almost as accurate:

$$\theta_0 = \frac{14.1\text{MeV}}{pv}\sqrt{\frac{L}{L_R}}\left[1+\frac{1}{9}\log_{10}\left(\frac{L}{L_R}\right)\right]\text{rad}. \tag{1.1}$$

Highland's formula gives the scattering angle θ_0 as a function of pv, which is the momentum of the protons times their velocity also known as the kinematic factor, L being the thickness of the target, and L_R the radia-

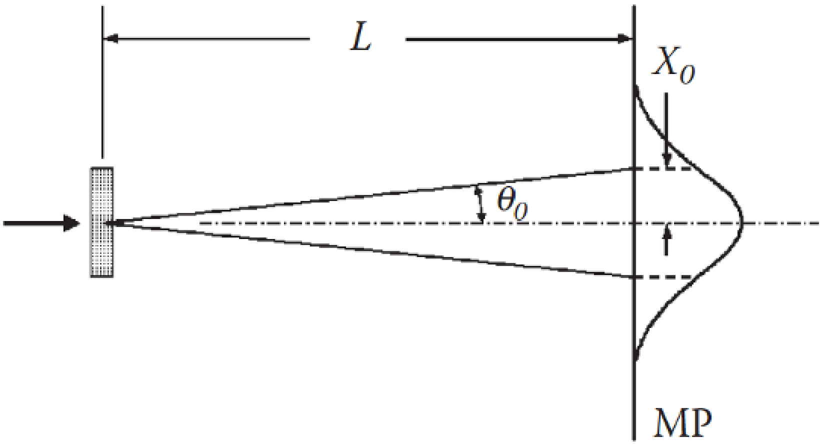

Figure 1.1: Multiple Coulomb scattering in a thin slab. MP, measuring plane. Figure taken from Paganetti [29].

tion length of the target material. The radiation length can be found in tables for different materials. It should be noted that equation 1.1 is only true for thin targets [16].

The nearly Gaussian beam profile has been explained to be shaped by MCS and single scattering. The single scattering accounts for the tails, but nuclear interactions also contribute to the beam profile in those regions. Nuclear interactions account for a halo in the beam profile, usually being greater than the single scattering tail. [31].

Nuclear interactions

Nuclear interactions are categorized in elastic collisions and nonelastic collisions. An elastic nuclear interaction takes place when a proton elastically scatters off a nucleus, with conservation of total kinetic energy and momentum. Nonelastic nuclear interactions are nuclear interactions where the total kinetic energy is not conserved. Nonelastic nuclear interactions occur when a proton has a head-on collision with a nucleus of the target, creating secondary particles, “secondaries”, with different energy and direction. Secondaries have lower energies and make large angles with the beam compared to primary protons, which is why nuclear interactions contribute to the tail regions of the beam profile and create a halo. A specific type of nonelastic nuclear interactions are inelastic nuclear interactions, which take place when an incoming proton knocks a proton out of the nucleus and replaces it. The nucleus before the collision will be the same as after the collision.

1.1.2. Energy deposition

Stopping

Stopping of protons occurs due to electromagnetic interactions, where the protons lose their energy and slow down in matter by collisions with atomic electrons. The less energy a proton has, the longer it will be close to the electron, increasing the transfer of momentum to the electron. As a result, the proton loses its energy faster as it slows down, leading to the Bragg peak shape, which will be explained later.

Range and stopping power

Range experiments give the distance a proton travels through a material before it stops [29]. The range can be measured by letting a proton beam traverse a material of a certain thickness and detect how many particles are left. Repeating this experiment whilst increasing the thickness, a graph can be made of the number of detected particles versus the material thickness. An example of such a graph can be seen in figure 1.2. The figure shows the results of a range experiment performed with two different Faraday cups to detect the particles. It can be seen that the detected number of particles decreases slowly at first, which is explained by nonelastic nuclear interactions. Secondaries have short ranges and travel at large angles, and will not reach the detector, depending on the sensitive area of the detector. The sharp decrease of the particles which can be seen at the end of the graph is caused by protons that lose energy by electromagnetic interactions and eventually stop.

The range R_0 of the protons is defined as the depth at which half of the protons have stopped. This point is shown by the arrow in figure 1.2. The nuclear interactions are left out of consideration to determine the range. Stopping power, denoted as S, is the rate at which a proton loses its kinetic energy in matter and can be described by the Bethe-Bloch formula, which for an elementary material reads [6, 13]:

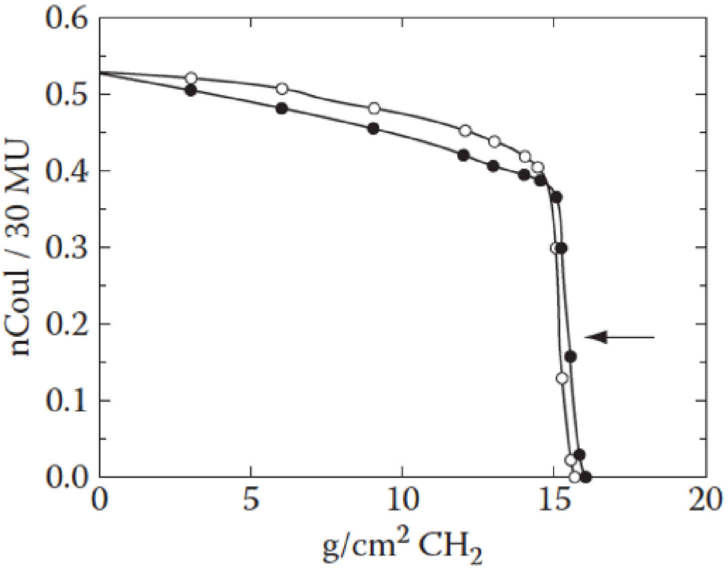

Figure 1.2: Results of a range experiment performed with two different Faraday cups. On the x-axis the thickness of the material is given and on the y-axis the proton fluence. The arrow indicates the point where half of the protons have stopped. Figure taken from Paganetti [29].

$$\frac{S}{\rho} \equiv -\frac{1}{\rho}\frac{dE}{dx} = 0.3072\frac{Z}{A}\frac{1}{\beta^2}\left(\ln\frac{W_m}{I} - \beta^2\right)\frac{\text{MeV}}{\text{g/cm}^2}, \tag{1.2}$$

where $\frac{S}{\rho}$ is the mass stopping power, ρ the density, Z the atomic number, A the relative atomic mass, and I the mean excitation energy of the material. $\beta \equiv \frac{v}{c}$ is the velocity of the proton divided by the speed of light, and:

$$W_m = \frac{2m_e c^2 \beta^2}{1-\beta^2}, \tag{1.3}$$

where $m_e c^2$ is the rest energy of an electron. It must be noted that the Bethe-Bloch formula as seen in equation 1.2 is in simplified form, as it is filled in for protons and physical constants. Also, density and shell correction factors are ignored, which is allowed for particles in the radiotherapy energy range (3-300 MeV) [27, 29].

Knowing the stopping power will make it possible to calculate the theoretical range R of a proton:

$$R\left(E_{initial}\right) = \int_{E_{final}}^{E_{initial}} \frac{dE}{S/\rho}. \tag{1.4}$$

This equation is based on a proton with energy $E_{initial}$ entering a material divided in slabs, calculating the energy loss in every slab and summing this until the proton has a very low final energy E_{final} close to 0. In practice the stopping power and range are retrieved by making use of range-energy tables and interpolating them. It is recommended not to do a linear interpolation, but instead use a power law [8, 29].

Sometimes it is preferred to know the water equivalent depth of a material, as water is often used as a substitute for tissue in calculations [50]. The water equivalent depth can be computed in case the relation between the range and energy are known for both water and the material of interest. The water equivalent depth or thickness (WET) t_w for a material of thickness t_m can then be calculated by:

$$WET\left(E\right) = t_w\left(E\right) = t_m \frac{\rho_m}{\rho_w}\frac{S_m\left(E\right)}{S_w\left(E\right)}, \tag{1.5}$$

where ρ_m and ρ_w are the density of the material and water, and S_m and S_w the stopping power of the material and water, which depend on the proton energy E.

The depth-dose curve: Bragg peak

The absorbed dose D equals the amount of energy absorbed per unit mass of the target. D has SI units [J/kg], but in practice the unit Gy is used. The depth-dose distribution of a proton beam in water is called the Bragg peak (BP). Figure 1.3 shows the characteristic shape of a Bragg peak. At the entrance a small build-up region can be seen followed by the plateau region with the contribution of nuclear interactions. The peak comes from the increase in rate of energy loss as the protons slow down, with eventually all protons having lost their energy causing the dose to drop to 0. The d_{80} and d_{20} are the depths at which the distal region of the peak reaches 80% and 20% of the maximum dose respectively. In depth-dose curves the equivalence of the range is the d_{80}, which is equal to the R_0 from range experiments. The distance between the d_{80} and the d_{20} is also known as the distal falloff. The width of the BP depends on range straggling (also called energy straggling) and beam energy spread. Energy straggling is caused by energy loss of a proton beam coming from many interactions affected by statistical fluctuations, resulting in the broadening of the Bragg peak. It will cause a range uncertainty as well and for this reason the range is also called the mean projected range.

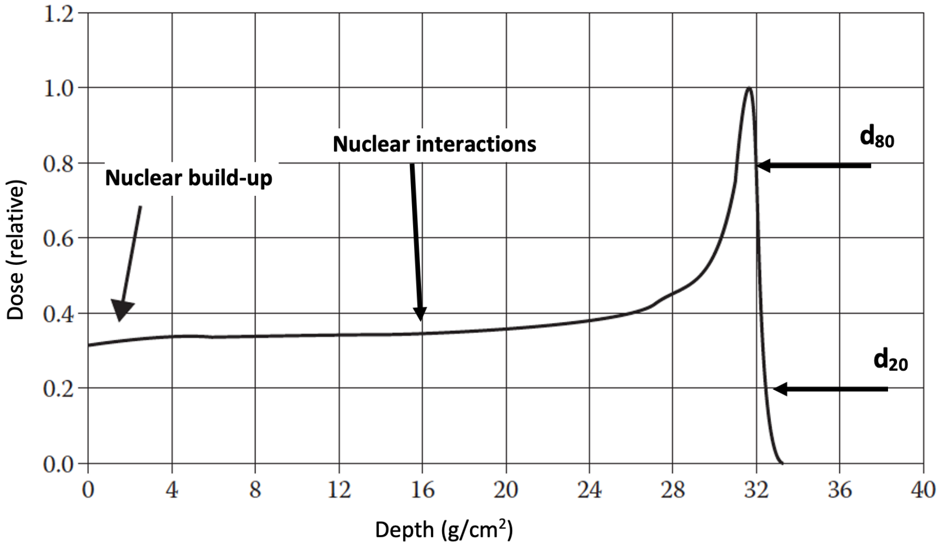

Figure 1.3: Depth-dose curve of a proton beam. Regions with nuclear build-up and nuclear interactions are marked, as well as the d_{80} and d_{20}. Figure taken from Paganetti [29].

1.2. Cyclotron systems

Now that the physics of proton beams are known in terms of interactions with materials and how these affect the lateral spread and BP, the production of the proton beam will be explained. As HollandPTC is equipped with a cyclotron, the working principle of these accelerators is described in this section.

1.2.1. Cyclotrons

A cyclotron is a particle accelerator and in the field of proton therapy used to accelerate protons to a fixed energy of up to 250 MeV. The produced proton beam is nearly continuous with an adjustable current. The main components of a cyclotron are a radio frequency (RF) system, magnet, proton source, and an extraction system. The RF system consists of two or four Dees coupled to an RF generator. A Dee is a pair of copper plates on top of each other with a couple of centimetres in between, connected at the outer edges. The Dees are positioned between two magnet poles, with a small gap in between the Dees. The RF generator will apply an oscillating voltage across the Dees, between 30 and 100 kV, with a certain frequency between 50 and 100 MHz. This induces an alternating electric field between the Dees. The protons that come from a proton source in the center of the cyclotron will be accelerated in each gap. The magnetic field makes the protons follow a circular trajectory. Protons that have reached the maximum energy get extracted from the cyclotron.

Extraction is done by a septum, which is a thin blade, that is placed parallel to the proton beam at the radial position where the protons have the right energy to get extracted. At a larger radial position parallel to the septum, a cathode is placed. The electric field between the septum and the cathode will deflect the beam to an extraction channel. A schematic view of some of the components can be seen in figure 1.4. This figure shows a system with two Dees, with the dotted line representing the trajectory of the protons.

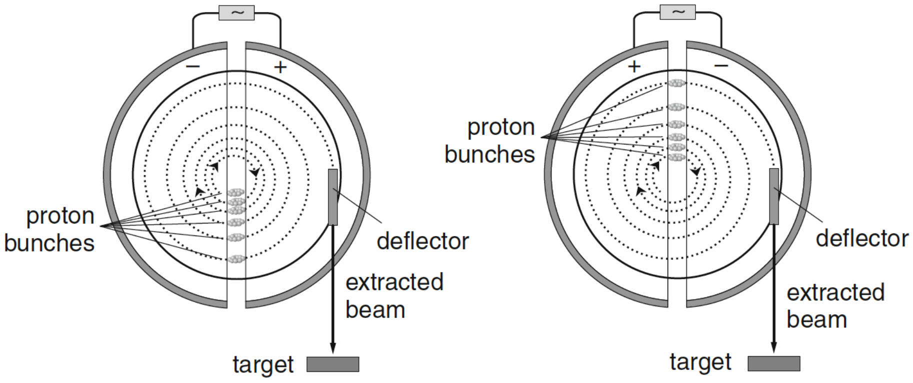

Figure 1.4: Schematic of part of a cyclotron system with two Dees. Showing the RF system, proton bunches and their trajectories, and beam extraction. The difference between the left and right image is the polarity of the Dees. Figure taken from Amaldi [1].

1.2.2. Beam transport

A schematic of a beam transport section is shown in figure 1.5. In the extraction channel steering, focusing, and defocusing is done by either permanent magnets or iron shaping blocks. The protons leave the cyclotron with a fixed energy, but the energy can be adjusted after extraction. This is effected with a degrader which is usually made out of carbon wedges. The thicknesses are variable such that the proton beam can be reduced

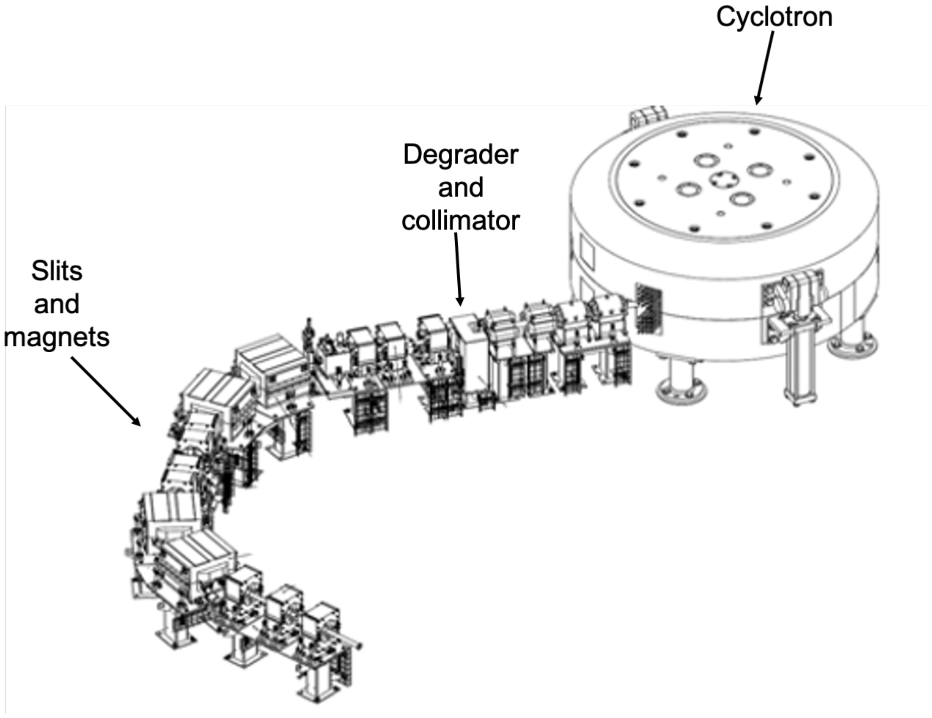

Figure 1.5: Schematic of a beam transport system for a proton beam exiting a cyclotron. The transport system includes the energy selection, focusing, and steering elements. The parts with the degrader and the energy selection system are shown by the arrows. Figure taken from Sichelbaut et al. [40].

to the desired energy. As the degrader lowers the energy of the proton beam, at the same time it will cause the beam to laterally increase in size. Additionally, there will be an increase in terms of the beam energy spread. To restore the beam quality, an energy selection system (ESS) is used [29, 40]. This system consists of collimators, slits, and magnets. From the ESS the beam is directed to the treatment room by a beam transport system in vacuum. Along the beam line more magnets are used for focusing and centering of the beam, together with beam monitors to monitor the beam. All of this is done to obtain the right beam characteristics, which include the beam energy, spot size, and current.

1.3. Passive scattering

The proton beam exits the beam transport system through the exit window. Near that moment it typically has a lateral spread of a couple of millimetres and is mono-energetic [29]. For dose delivery with full coverage of targets, the beam needs to be spread laterally to achieve a uniform area in the lateral direction, except in the case of magnetic scanning systems. Moreover, spreading of the beam in depth direction is needed to achieve full 3D coverage, which can be achieved by adding shifted BPs [8]. A widely used method to do this is passive scattering.

1.3.1. Passive scattering techniques

Single scattering

The simplest way to laterally broaden a proton beam is by a single flat scatterer, typically made of a high-Z material [29]. Single scattering makes use of MCS to broaden the beam. This technique has the same working principle as was shown in figure 1.1. As the aim is to uniformly cover the target, the scattered field should have a high uniformity, typically 97-98% [14, 29]. After the flat scatterer the field will be of nearly Gaussian shape. To create a sharper lateral penumbra a collimator has to be placed in front of the target. A schematic representation of a single scattering system is presented in figure 1.6. A drawback of single scattering is the low efficiency, which means that high beam currents are needed. High beam currents result in more secondary neutrons being produced in the scattering material, which is a con in terms of radiation safety. This is why single scattering is only used to create small fields with a diameter of up to 7 cm [29]. An advantage however is the sharp lateral penumbra which can also be observed in the schematic.

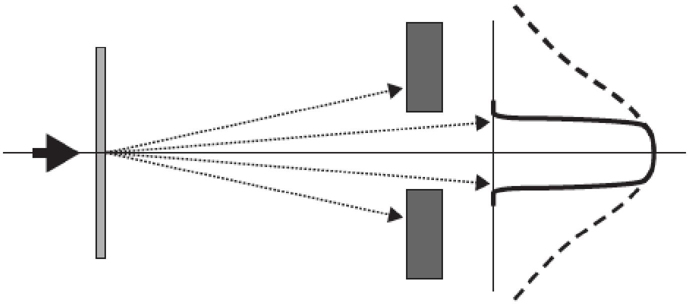

Figure 1.6: Schematic representation of single scattering with a flat scatterer. The beam gets scattered by the flat scatterer and then shaped by a collimator. The lateral profile after the collimator is the solid line. The dashed line shows the lateral profile for a setup without a collimator. Figure taken from Paganetti [29].

Double scattering: Dual ring

Double scattering makes use of a flat scatterer that spreads the beam, which then gets further scattered by a second scatterer. Several double scattering setups exist, but for the purposes of this thesis the double scattering technique with a dual ring setup will be explained [41]. A dual ring scatterer is a disk of a high-Z material, surrounded by a ring of a lower-Z material. The idea behind this design is that the first scatterer produces a broad Gaussian profile, which falls on the dual ring. The inner disk will again produce a Gaussian profile, and the ring around it will produce an annulus-shaped profile. These profiles combined will give a uniform profile. Again, for a sharper lateral penumbra a collimator can be placed in front of the target. Figure 1.7 shows a schematic of the working principle of a dual ring setup. A drawback of the dual ring setup is the high sensitivity to beam misalignment. Furthermore, if the field falling onto the second scatterer is too big, the resulting profile will have “horns” and if it is too small the shape will be “domed” [29].

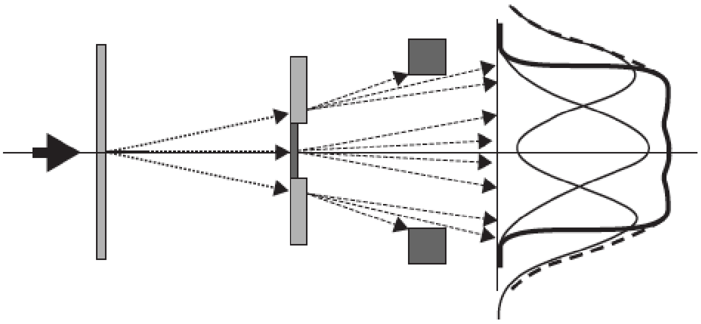

Figure 1.7: Schematic representation of double scattering with a dual ring setup. The beam gets scattered by the flat scatterer, falls onto the dual ring, further scattering the beam, which is then shaped by a collimator. The lateral profile after the collimator is the solid line. The dashed line shows the lateral profile for a setup without a collimator. Figure taken from Paganetti [29].

1.3.2. Range modulation: Ridge filter

From figure 1.3 it can be seen that for coverage of a target in depth, a single BP will be too sharp. A way to overcome this is by range modulation, which is the combination of BPs of different beam energies [10]. Giving each BP a suited weight will result in a uniform depth-dose region in the depth-dose curve. This region is called a spread-out Bragg peak (SOBP). Figure 1.8 shows a 10 cm SOBP and how it is the result of weighted BPs. For the optimal weights of the BPs for a SOBP, measured BPs are used to numerically determine these weights. In proton therapy different range modulation methods exist. As for this thesis the ridge filter method is used, this technique is explained in the next section.

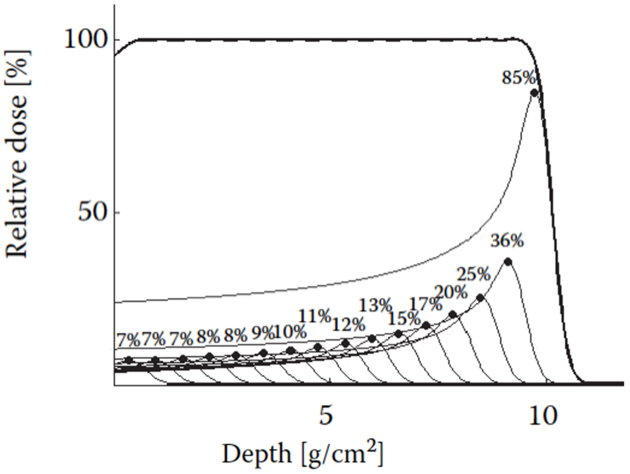

Figure 1.8: Depth-dose curve of a SOBP of 10 cm wide, showing how it is the result of combining different weighted BPs. Figure taken from Paganetti [29].

Ridge filters

A type of ridge filter is shown in figure 1.9 together with the design of a single ridge [20]. The idea is that protons that hit the highest point of the peak will lose the most energy and determine the most proximal BP. Protons not hitting the ridge will lose the least energy and determine the most distal BP. The protons hitting the other parts of the ridge will form all the BPs in between. The thicknesses and the widths of the steps in the ridge determine the uniformity of the SOBP, which should typically be at least 98% [29]. Designing a ridge filter has some constraints. Firstly, ridges should not be too sharp, as they will be difficult to manufacture. Secondly using high-Z materials will result in a larger lateral penumbra. Nowadays as manufacturing techniques have improved, it is possible to manufacture ridge filters made out of lower-Z materials, which even include some plastics [39].

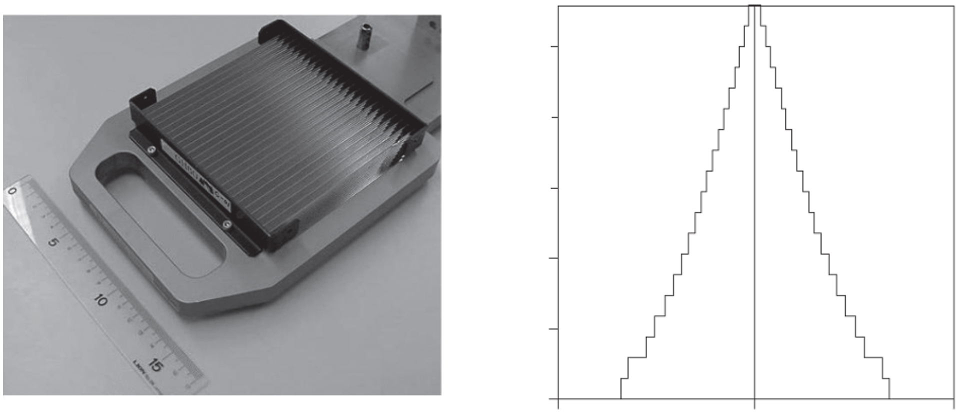

Figure 1.9: Left: Bar ridge filter. Right: schematic of the cross section of a ridge. Figures taken from Paganetti [29].

1.4. Summary

Proton interactions with matter are explained together with the working principle of a cyclotron system. This explains how the characteristics of a beam are formed from the cyclotron extraction all up to the target. Additionally, the characteristics are of importance for designing a passive scattering setup. Next a literature study has been done to determine which methods can be used for the proton beam characterization at the experimental room of HollandPTC and which ones are the best in terms of accuracy, speed, and complexity.

2

Literature Study

This chapter is a shorter version of the literature study "Methods of proton beam characterization". The literature study has been part of the master thesis and focuses on different methods to fully characterize the proton beam. The goal is to have a broad overview of the different techniques used for proton beam characterization and to compare the approaches used in different facilities worldwide. Emphasis will be on beam profile, beam envelope, and beam current, as well as Bragg peak measurements and energy spread. First the methodology of the literature study is presented, after which the methods found for the characterization in literature are being discussed.

2.1. Methodology

For this literature study WorldCat Discovery – TU Delft, PubMed, Web of Science Core Collection, and Scopus databases have been consulted. The key phrases that have been used are summarized in table 2.1:

Table 2.1: Key Phrases used for searching in the databases.

Group	Key phrases
1	'protonbeam' 'proton beam'
2	'characterization' 'characterisation'
3	'profile' 'envelope' 'Bragg peak' 'flux' 'energy spread'

"OR" operators have been placed within the groups and "AND" operators have been placed between the groups with the following combinations: Group 1+2 and Group 1+2+3. The articles shown in the results have been selected based on the abstract. The aim was to select articles with a diversity of characterization methods. Articles that showed too many similarities to the ones already selected were excluded. Additionally, the book Proton Therapy Physics by H. Paganetti [29] has been used to gain more background information on the topics.

2.2. Proton beam characterization in literature

2.2.1. Beam profile measurements

Several methods for beam profile measurements have been found in literature. One method is by using a Gafchromic (EBT3) film, which changes colour in regions where it is exposed to ionizing radiation. In this way one can make a 2D image of the beam spot. It can be used in combination with a scanner or camera to digitize the beam spot image. The resolution will depend on the type of scanner or camera that is used. Lin et al. [21] uses Gafchromic films to characterize 2D spot profiles. Pencil beams between 100 and 225 MeV were characterized in air and in a Solidwater® phantom. In this case the Gafchromic films were used together with a commercial flatbed scanner with 0.5 mm spatial resolution. Park et al. [30] used radiographic films as well to study the beam profile of a collimated proton beam and to determine the beam divergence, which is the increase of the beam size with distance. Park et al. [30] did this by measuring the beam spot size at a certain distance from a 2 mm carbon collimator. Figure 2.1 is an example of how a radiographic film looks after proton irradiation. A clear Gaussian beam spot can be seen together with the halo due to nuclear interactions.

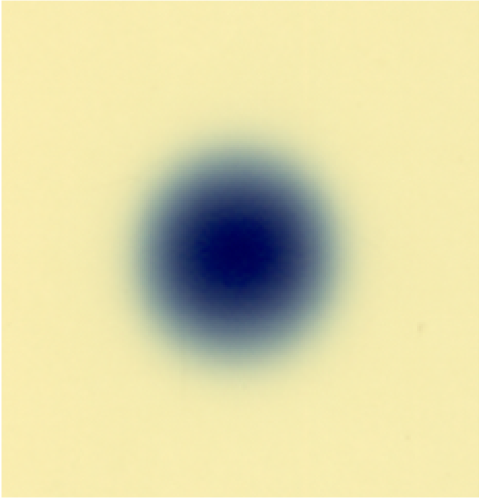

Figure 2.1: Example of a scanned Gafchromic film irradiated with a 150 MeV proton beam. Courtesy of M. Rovituso.

Sawakuchi et al. [36] made use of Gafchromic films for measuring the profile of a single pencil beam (72.5 – 221.8 MeV). In this case the Gafchromic films were used as an extra check for the ionization chamber (IC). The measurements were done in air and the films were scanned with a commercial flatbed scanner, giving a spatial resolution of 0.35 mm. An example of a profile Sawakuchi et al. [36] measured can be seen in figure 2.2.

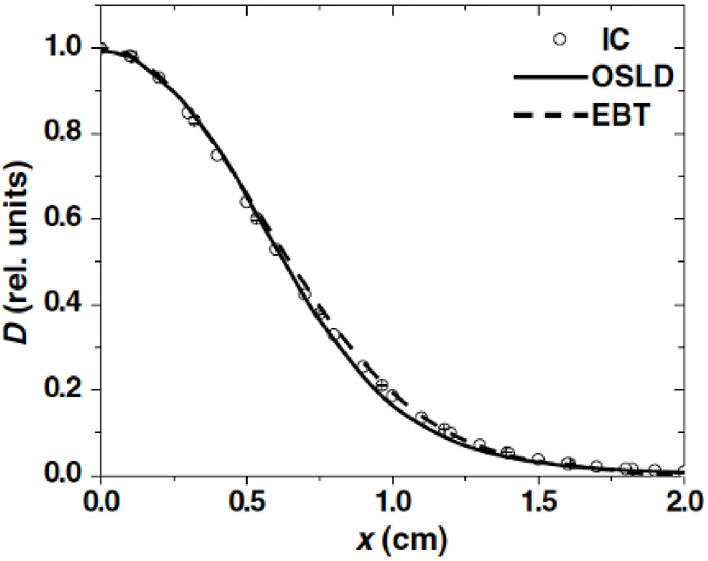

Figure 2.2: Lateral profile in air at the isocenter of a 228.1 MeV pencil beam measured with an IC, optically stimulated luminescent detector (OSLD), and a Gafchromic film (EBT) measured and shown by Sawakuchi et al. [36].

As seen previously, the Gafchromic films are not always used on their own to measure the beam profile, but usually as “cross-check” or calibration tool. Bisogni et al. [7] used a Gafchromic film (digitized with 0.2 mm spatial resolution) as a control of their detection system to measure the beam profile of a (collimated) 62 MeV proton beam. The system was proposed for online beam characterization. It is based on a silicon pixel detector coupled to a single event counter read-out chip Medipix2. The read-out chip consists of 256 x 256 cells and the detection surface is 2 cm2 with 55 μm spatial resolution. The read-out of all the cells together would give a 2D beam spot and the results of the beam profile in the x-direction can be seen in figure 2.3. After analysing the beam spot measured with the Medipix2 system, it was compared with the Gafchromic film, showing comparable results within the error bars.

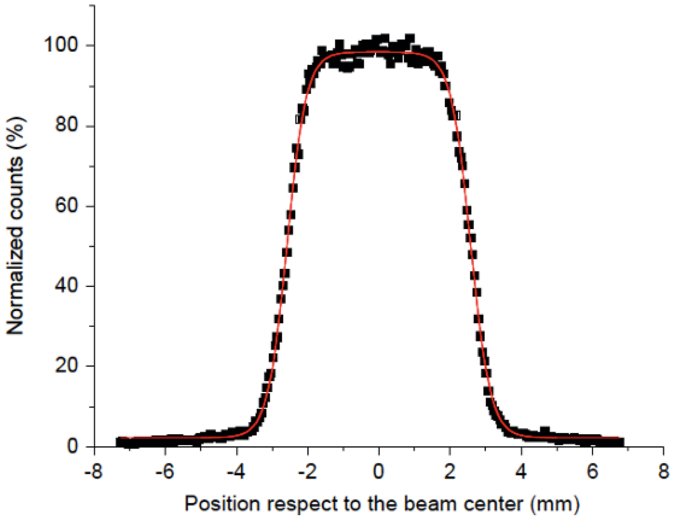

Figure 2.3: Beam profile in x-direction of a 64 MeV collimated proton beam measured with Medipix2. The red line is a fit. Measured and shown by Bisogni et al. [7].

Another way to measure the beam profile is to use different types of ICs. Schwaab et al. [38] used 24 PinPoint ICs, which are small ionization chambers, to measure beam profiles in air and in water. The setup of these ICs can be seen in figure 2.4. A lateral precision of 0.5 mm has been achieved with this setup.

Figure 2.4: Setup of measuring lateral beam profiles in air with 24 PinPoint ICs by Schwaab et al. [38].

The PinPoint IC was used by Sawakuchi et al. [36] too, but instead of putting multiple ones next to each other to measure the beam profile as in [38] Sawakuchi et al. [36] used one PinPoint IC and would move it in small steps of 0.1-1.0 cm to measure the profile of the pencil beam, giving a 1 mm spatial resolution when using the smallest step size. The results of these measurements with the PinPoint IC can be seen in figure 2.2 that was shown before.

Tommasino et al. [42] characterized the “Physics” experimental beam line in the proton therapy facility in Trento. The Physics beam line consists of a fixed single pencil beam. The beam profile measurements were done with a Lynx (IBA-Dosimetry) detector, which consists of a scintillating screen (sensitive area of 30 x 30 cm, 0.5 mm spatial resolution) that is coupled with a CCD camera to measure 2D beam spot profiles in air for beam energies ranging from 70 to 228 MeV. Some beam profiles that are measured at the isocenter for different beam energies can be seen in figure 2.5.

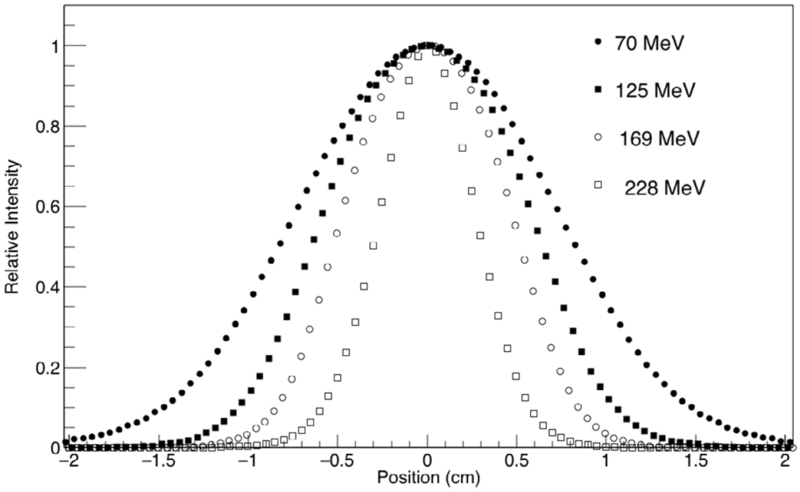

Figure 2.5: Beam spot profiles measured at the isocenter. Measured and shown by Tommasino et al. [42].

Piccinini et al. [32] used a solid-state radiation detector for measuring the beam profile during the commissioning of a 150 MeV proton linear accelerator. The experiments took place up to the 27 MeV segment. The detector material consists of lithium fluoride (LiF). When ionizing radiation (in this case the proton beam) penetrates the LiF crystal, F_2 and F_3^+ colour centers (CCs) are created, which are laser-active electronic defects. The concentrations of F_2 and F_3^+ are proportional to the deposited energy in the crystal. Piccinini et al. [32] present results of using LiF crystal radiation detectors based on the photoluminescence (PL) of CCs for proton beam characterization. The resulting 2D image can be read out by a fluorescence microscope. Images with a pixel size of 1.63 μm were made. A PL image of the LiF crystal irradiated with a 7 MeV proton beam can be seen in figure 2.6.

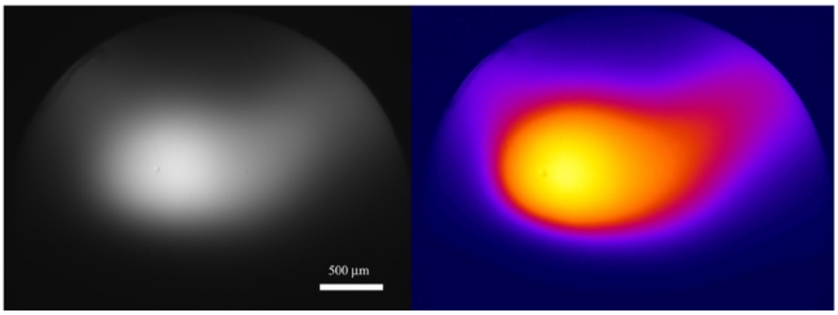

Figure 2.6: PL image of a LiF crystal irradiated with a 7 MeV proton beam, with the right one in false colour to show intensity differences. Measured and shown by Piccinini et al. [32].

For the characterization not only the (2D) beam profile is needed, but also its analyses and parametrization. Since Monte Carlo simulations are not fast enough, treatment planning systems (TPS) use parametrization of the beam profile to calculate plans for patient treatment. As explained before and shown in 1.1 the beam profile is nearly Gaussian due to MC scattering and often measured profiles are fitted to a single Gaussian [4, 38]. However, the single Gaussian does not include nuclear interactions, so in most modern treatment planning systems the profiles are approximated by a sum of Gaussians (double Gaussian for protons). A trade-off has to be made between computation time and accuracy. When the tails are not parametrized correctly however, this will result in an incorrect estimation of the delivered dose. Bellinzona et al. [4] have been looking into improving the description of the tails of the beam profile by looking into alternative functions and at the same time taking the efficiency into account. It has been concluded that a triple Gaussian, and double Gaussian-Lorentz Cauchy functions gave the best results. Both functions however contain six parameters. A double

Gaussian and Gauss-Rutherford on the other hand gave comparable results, both having four parameters, and needing less computational time.

2.2.2. Beam envelope measurements

The beam envelope is the evolution of the beam profile in a material as a function of distance from the exit window [42]. Practically, it is the measurement of the beam spot size at different depths in air or phantom. Lin et al. [21] performed measurements of the beam profile at different depths both in air and in a Solidwater® phantom using Gafchromic films. One of the results of the envelope measurements in the Solidwater® phantom can be seen in figure 2.7. In this figure the FWHM of the beam spots can be seen. It clearly shows that the FWHM increases until the end of the range and then decreases as the distal falloff region is reached.

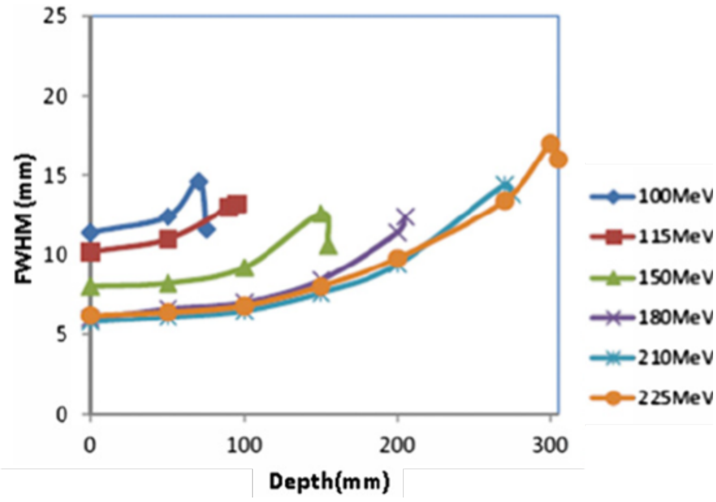

Figure 2.7: Full width at half maximum for pencil beams of different energies in different depths of a Solidwater® phantom until the end of their range with the phantom surface at isocenter. Measured and shown by Lin et al. [21].

Sawakuchi et al. [36] also studied the beam envelope of the proton beams in air and in water by using the PinPoint IC. Results of Sawakuchi et al. [36] can be seen in figure 2.8. In figure 2.8 the FWHM of three pencil beams of different energies are shown, measured in different depths in air. Together with the data points, they show the parameters of a linear fit to those points. It can be seen that the beam spot size increases downstream (z<0) of the isocenter and decreases upstream (z>0) of the isocenter. This means that the ion optics are set to deliver a diverging beam.

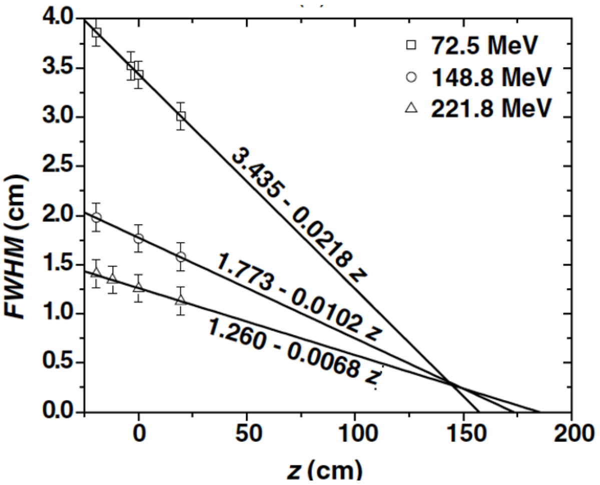

Figure 2.8: Measured and fitted full width at half maximum (FWHM) for different pencil beam energies at different depths in air. z=0 is at the isocenter plane. Positive z means upstream the beam direction and negative z downstream the beam direction. Measured and shown by Sawakuchi et al. [36].

Bisogni et al. [7] were interested in the broadening of the beam passing through PMMA of different thicknesses, using the same detection method described earlier in section 2.2.1. They measured the lateral penumbra, which is the distance between the points at 80% and 20% of the normalized profile. Furthermore Bisogni et al. [7] compared the measured results with GEANT4 Monte Carlo code simulations. The results can be seen in figure 2.9. This figure clearly shows the broadening of the lateral penumbra as the beam travels through more PMMA and also the comparison between the experimental data and the calculated data.

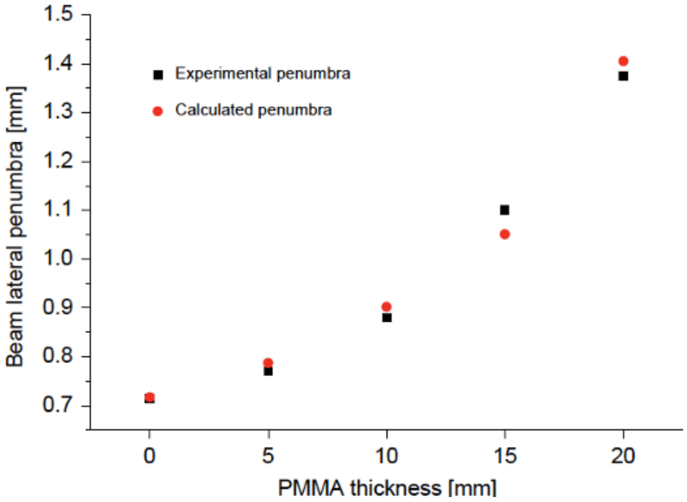

Figure 2.9: Beam lateral penumbra in x-direction for increasing PMMA thickness. Measured and shown by Bisogni et al. [7].

Tommasino et al. [42] used the Lynx detector to do spot profile measurements of the single pencil beam at different distances from the exit window. Assuming the profiles are Gaussian, the beam width (defined as sigma) has been plotted as a function of distance from exit window for different energies. The plot for the 70 MeV beam can be seen in figure 2.10. In this case it is possible to observe a divergent beam with focus point before the vacuum exit window which is set at 0 cm depth. Moreover, an asymmetry on the beam shape a few centimetres after the exit window can be appreciated. This effect is due to the ion beam optics settings which create an elliptic shape.

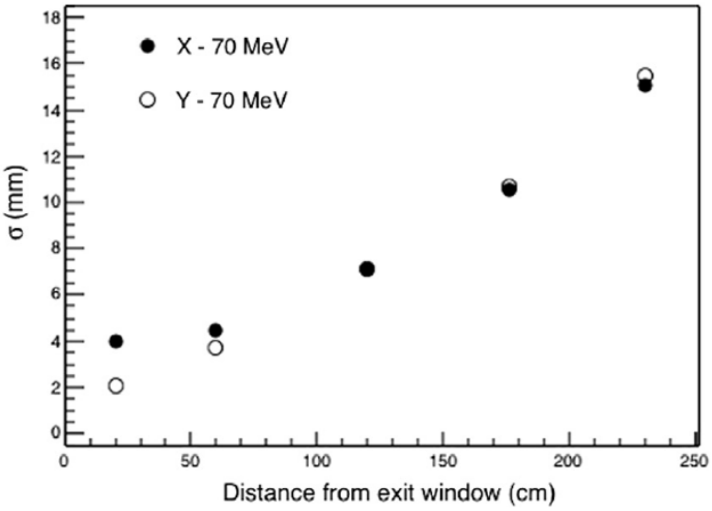

Figure 2.10: Beam width in x and y as a function from the exit window for a 70 MeV beam. Measured and shown by Tommasino et al. [42].

2.2.3. Beam current measurements

Particle flux is defined as the number of particles per second per unit of area. However, in literature the term flux is often used to indicate the number of particles per second. From now on we will indicate flux as the number of particles per second. The proton beam flux is an important characteristic, since the dose rate depends on it. It can be measured with different devices and one of those is the Faraday Cup (FC), which is a charge collector. It can be used as a proton counter since the charge of a proton is known [29]. Kim et al. [19] made use a FC to characterize a new low-flux proton beam (10^5 protons per second per pulse) of their new 100 MeV linear accelerator. They made use of a retractable FC, which is used to monitor the intensity of the beam. Nesteruk et al. [26] reported a study of an 18 MeV proton beam produced by a cyclotron. The beam currents were in the nA range and were measured by a FC at the end of the beamline.

Tommasino et al. [42] use a FC for cross calibration of the Mini-Q (DE.TEC.TOR) detector in their experiments. The Mini-Q detector is a multi-strip IC with strip chambers along the x- and y-direction. This means that it can be used for beam profile measurements. However, the Mini-Q contains one integral chamber, which can be used to measure the proton flux, after being calibrated. The measurements with the FC and Mini-Q have been done for a proton flux of 10^6-10^9 protons per second at the isocenter. For low proton flux (10^1 – 10^5 protons per second) measurements, a plastic scintillator coupled with a photomultiplier tube (PMT) has been used to measure the flux.

Bisogni et al. [7] were also interested in the applicability of Medipix2 as a single proton counter. To cross validate the concept a control system consisting of a (YAP:Ce) scintillating crystal was used. The beam was collimated to avoid pile-up problems. In that condition both systems measured a rate of 1.6 protons per second per pixel. After that measurement, the cyclotron current was increased up to clinical values (nA range). While increasing the current the number of counted protons by Medipix2 increased linearly. The flux measurements resulted in the conclusion that Medipix2 was suited to be used as a single proton counter.

2.2.4. Bragg peak measurements

A simple range experiment is described by Paganetti [29] where a monitored proton beam traverses through a material after which the beam gets collected in a FC. The material has an adjustable thickness, such that measurements at different target thickness can be made. A schematic setup can be seen in figure 2.11. This range experiment is the same as the one described in section 1.1.2. The difference with a normal flux measurement is the fact that in a range experiment for each thickness a comparison is made between the flux of the incoming beam that is measured in the first detector and the flux that is measured in the second detector after the beam has passed a material. Tommasino et al. [42] used a Giraffe (IBA-Dosimetry) detector, which is a multilayer IC with 180 independent parallel-plate ICs, to do range experiments. The raw data resolution is 2 mm and each layer of the detector has a water equivalent depth, which is given by the manufacturer or can be calibrated. Tommasino et al. [42] compared the range measurements done with the Giraffe to range

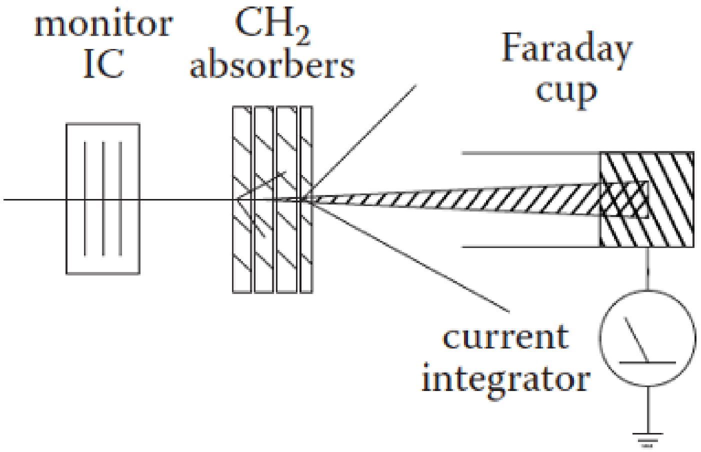

Figure 2.11: Setup of a range experiment. Figure taken from Paganetti [29].

measurements that have been done with a water phantom and a Bragg peak chamber. The measurements with the water phantom are done by measuring the intensity of a beam in a water phantom, that contains a reference IC where the beam enters the phantom. Results of the Bragg peak curves measured with the Giraffe can be seen in figure 2.12.

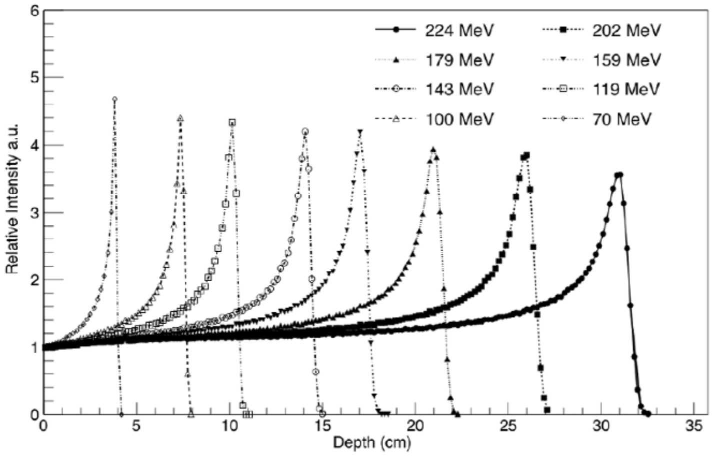

Figure 2.12: Bragg peak curves measured with the Giraffe detector. On the y-axis the relative intensity measured by the Giraffe detector is given and on the x-axis the depth in water. Measured and shown by Tommasino et al. [42].

Constanzo et al. [11] use a stack of depleted Silicon Surface Barrier Detectors (SSBD). The advantage of these detectors is that the entrance window is very thin, which means that almost no energy is lost in the window. The number of electron-hole pairs a proton creates in each detector is proportional to the energy the proton has lost. Constanzo et al. [11] compare the measured signal in all four calibrated SSBDs and obtain the initial beam energy. The initial beam energy of the 25 MeV proton beam was measured to be 24 MeV ± 0.14 MeV before the exit window. The uncertainty in the measurement came from residuals from the calibration curve that has been used.

Depth-dose curves were measured experimentally and compared to Monte Carlo (MC) simulations by Tommasino et al. [43]. The measurements were done with a Bragg peak ionization chamber inserted in a water phantom. This was both done with and without a modulator for a SOBP. The results of the depth-dose curves without range modulator can be seen in figure 2.13. It shows that the simulations were able to reproduce the measured data.

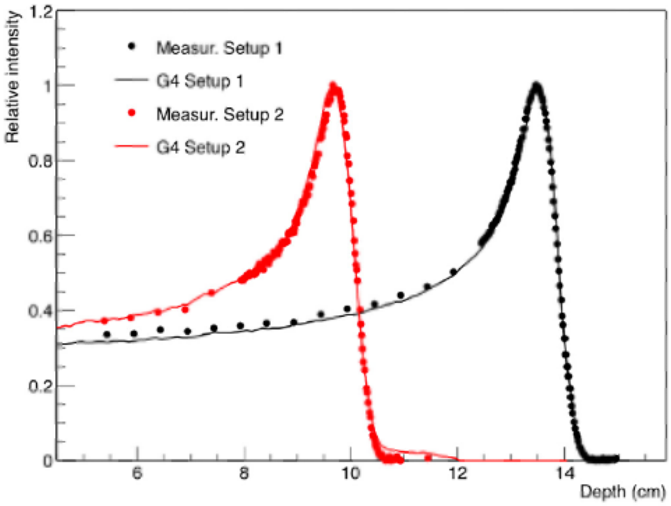

Figure 2.13: Measured and simulated depth-dose curves for a 148 MeV proton beam in two different setups. The two different setups correspond to setups used to create a big field (6 and 16 cm in diameter) by passive scattering. Tommasino et al. [43].

Microdosimetry looks at the effect of radiation at a microscopic level, in order to simulate the effect of radiation in the cell. Microdosimetry makes use of stochastic quantities that are equivalent to the macroscopic quantities. One of the microscopic quantities is lineal energy (equivalent to linear energy transfer (LET)). The lineal energy is the energy of a single event in a volume divided by its mean path length [29]. Tran et al. [45] used a microdosimetric kinetic model (MKM) to retrieve the RBE values of the BP. For the microdosimetric measurements a silicon on insulator (SOI) microdosimeter has been used, which was a 3D array of sensitive volumes. The thickness of each sensitive volume is of the order of 10 micron. The deposited energy by the protons (and secondary particles) in the array can be determined event by event. One of the advantages of a SOI microdosimeter is the high spatial resolution, which is of the order of 100 micron. The high spatial resolution is handy at the end of the Bragg peak. The microdosimetric probe was put in a water phantom and remotely controlled. The measurements have been done in a water phantom and the measured lineal energy (y_D) and the resulting depth-dose curve can be seen in figure 2.14. Additionally, Tran et al. [45] have done depth-dose measurements with the Zebra (IBA-Dosimetry) detector, which is similar to the Giraffe used in [42], and compared the results to Geant4 simulations. These results can be seen in figure 2.15. It shows that the simulations are corresponding to the measured data.

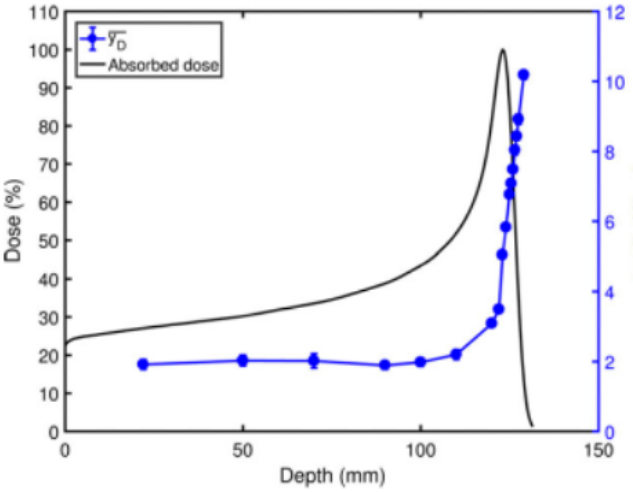

Figure 2.14: Depth-dose curve and lineal energy for a 131 MeV pencil beam in water. Measured and shown by Tran et al. [45].

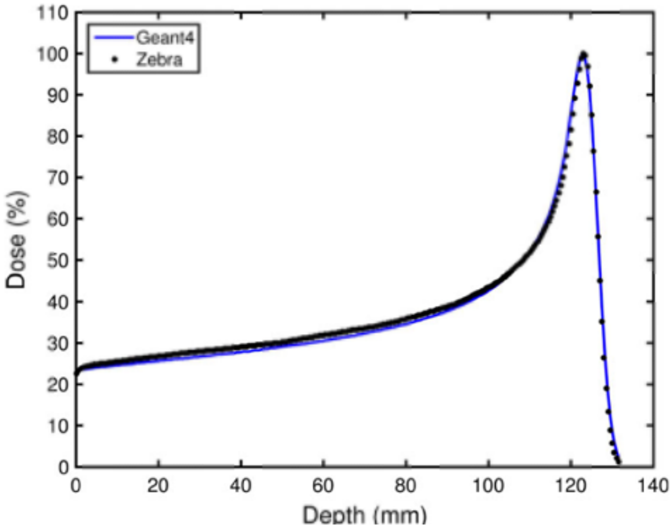

Figure 2.15: Depth-dose curve measured with a Zebra detector and Geant4 simulated curve. Measured and shown by Tran et al. [45].

Mirandola et al. [23] characterized a multilayer ionization chamber (MLIC) prototype, similar to the Giraffe and Zebra that were mentioned before. This MLIC is a module of the QUBE (DE.TEC.TOR) detector and is meant for integral ionization curves and SOBP measurements. It consists of a stack of 32 parallel plate ICs, and in each chamber a 1 mm aluminium plate is inserted as beam energy absorber and cathode. Beam energies in the range of 62.73 to 228.57 MeV were used to characterize the MLIC QUBE. The (water equivalent) spatial resolution was about 2.3 mm and the results of the characterization seemed promising for the MLIC QUBE.

Assmann et al. [3] used a completely different method than we have seen in this literature study until now. The Bragg peak is characterized with ionoacoustic waves. The energy loss of protons results in thermoacoustic signals, which can be measured with ultrasound detectors. The experimental setup for the experiments can be seen in figure 2.16. The authors conclude that this method of measuring the Bragg peak position is much simpler than the methods which are nuclear based. On top of that it can give the Bragg peak position with an accuracy below 100 microns. Van Dongen et al. [46] use ionoacoustics to reconstruct a 3D dose distribution for a modelled acoustic field in a heterogenous cancerous breast irradiated with an 89 MeV proton beam. The study is meant to show the possibilities of using ionoacoustics for monitoring the dose distribution during treatment of breast cancer. Van Dongen et al. [46] were able to reconstruct the position of the maximum amplitude of the dose distribution in the breast with an absolute error of 5.0 mm for an isochronous cyclotron and 5.2 mm for a synchrocyclotron.

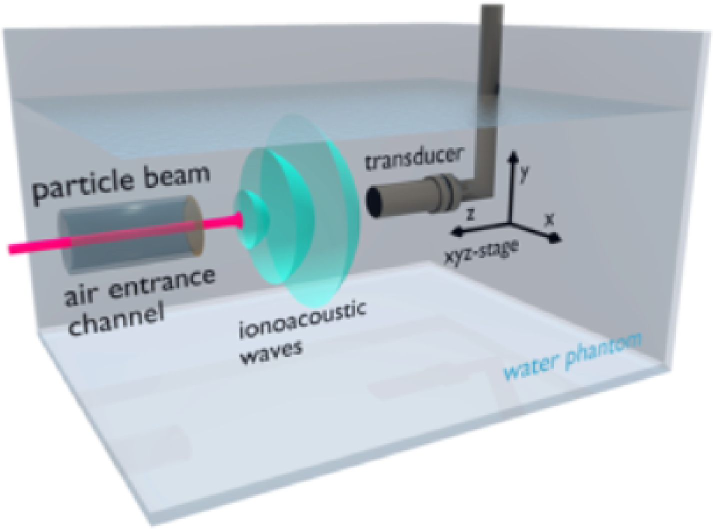

Figure 2.16: Experimental setup of ionoacoustic Bragg peak measurements by Assmann et al. [3].

Polge et al. [33] used optically stimulated luminescence (OSL) films. When an insulator is irradiated with ionizing radiation, charges will get created in the oxide and some charges will stay trapped locally. When the material is thermally or optically stimulated, the trapped particles get released and can result in radiative recombination. The photons that get emitted are proportional to the absorbed dose. Polge et al. [33] irradiated seven OSL films that were inserted between plates of plexiglass. By analysing the irradiated OSL films the depth-dose or Bragg peak curves were retrieved. The obtained depth-dose curve can be seen in figure 2.17. The measurements have been compared to results obtained with a diode. Polge et al. [33] concluded that the method of using seven OSL films was accurate to an extent, but not able to provide an exact position of the Bragg Peak.

The use of plastic scintillator dosimeters has been studied in the past by Torrisi [44] but they have not been used widely. Plastic scintillators have had advantages in photon and electron therapy such as high sensitivity, spatial resolution, and water equivalence. However, in proton therapy they have a quenching effect, where the output depends on the incident energy. Archambault et al. [2] studied the applicability of miniature plastic scintillators detectors to proton therapy. They chose to do the study by MC simulations in a large number of different experimental situations, to overcome the limited research time in a clinical proton facility. They did this for two types of plastic scintillators: the first one is a piece of plastic containing scintillating solutes. The second one is a scintillating fiber consisting of a piece of polystyrene and surrounded by non-scintillating plastic cladding. The simulated scintillators were cylindrical in shape. The simulations showed that adding

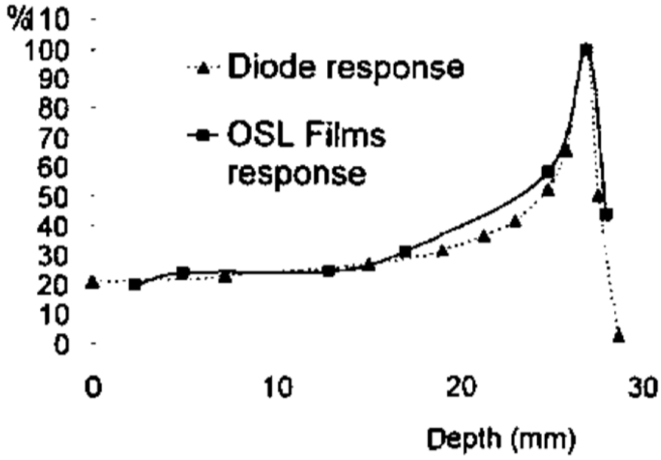

Figure 2.17: Depth-dose curve in plexiglass, obtained by OSL films and compared to diode measurements. By Polge et al. [33].

a reflective coating to the plastic scintillator would increase the signal amplitude by a factor of 2 for the first type of plastic scintillators and a factor 4 for the second type of scintillators. Additionally, for proton beams of 100 MeV or higher the radius of the scintillators should be 0.5 mm at maximum to be able to measure the Bragg peak accurately. There is, however, a trade-off between radius and signal, so also here the reflective coating would be an outcome. Moreover, for better depth-dose resolution a thinner scintillator would be the best solution. Archambault et al. [2] proposed a rectangular slab of 0.25 mm or less in thickness and a width of the order of millimetres. The quenching effect mostly was a problem close to the Bragg peak, so plastic scintillators would be more suited for superficial dose measurements. However, with simple models it was possible to accurately predict quenching. That is why Archambault et al. [2] believes that the quenching effect can be corrected by determining depth-correction factors with MC simulations and make use of plastic scintillators for deeper depth-dose measurements.

The solid-state detector that Piccinini et al. [32] used for the beam profile was also used to perform Bragg peak measurements. When using the same LiF crystal, which is 10x10 mm2 and 1 mm thick, with the 10x10 mm surface parallel to the beam direction and the side perpendicular to the beam axis, it is possible to image the Bragg curve. The spatial resolution of this method is ±1 pixel (1.63 μm). The uncertainty in the position of the Bragg Peak with these measurements is ± 7 μm total including the spatial resolution and the uncertainty of the position of the crystal edge. One of the images can be seen in figure 2.18. The intensity of the image is proportional to the deposited energy and in that way the Bragg curves are obtained.

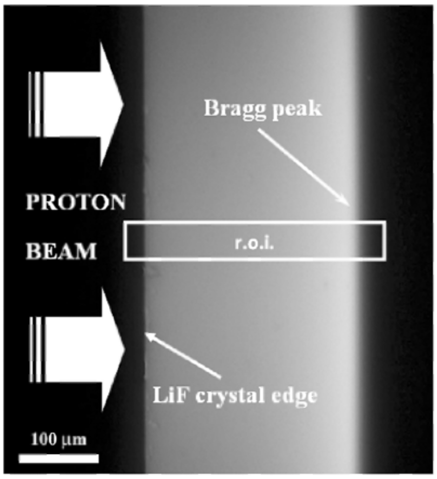

Figure 2.18: Photoluminescence image of the Bragg curve of a 7 MeV proton beam stored in a LiF crystal detector. Presented by Piccinini et al. [32].

Warman et al. [47] looked at the potential of an organic radio-fluorogenic gel for 3D dose monitoring with submillimeter resolution. Fluorescent images of the track of an 80 MeV proton beam were made. Figure 2.19 shows an image of the gel after exposure to the beam. The image clearly shows the diverging beam as it passes through the gel and the increase of intensity in depth until the Bragg peak. Warman et al. [47] concluded that the method had potential for making 3D images, which show the dose distribution in depth and also the lateral dose distribution. Luthjens et al. [22] made an eye phantom of the same radio-fluorogenic gel as Warman et al. [47] and looked into the possibilities of using the phantom for monitoring the proton beams used in ocular radiotherapy. In the study 3D images were made of an x-ray beam and it was shown that it was possible to make those images within minutes of irradiation. The intention is to use the same method for proton pencil beams.

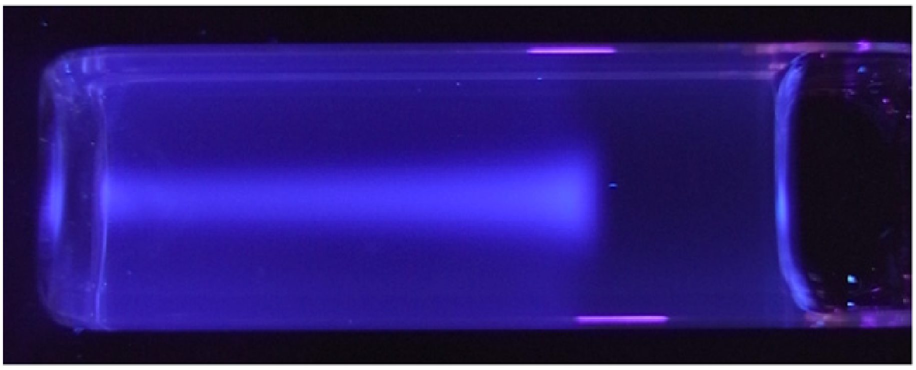

Figure 2.19: Image of a 58 mm long radio-fluorogenic gel sample after irradiation with an 80 MeV proton beam. Made by Warman et al. [47].

The energy spread of a proton beam entering the nozzle coming from a cyclotron is usually less than 1%, but it will increase when a proton beam passes a material. An example is when a degrader scatters the proton beam. An increase in energy spread will increase the range straggling. The energy spread can be estimated from pristine Bragg measurements [29]. Tommasino et al. [42] calculate the Delta R80 of the Bragg peak and state that the value gives an indication of the energy spread. The Delta R80 is the distance between the proximal and distal depths where the dose is equal to 80% of the maximum dose. Furthermore, Bragg peak curves have been simulated with Monte Carlo simulations and comparing those with the measured Bragg curves showed that the beam initial energy spread ranged between 0.7% and 0.3%.

2.2.5. Overview characterization methods

Table 2.2 shows a summary of all the methods described above. The first column describes the type of measurements, the second one lists the names of different methods, the third one gives the resolution of the method, and the fourth one collects the bibliography. The resolutions for the beam profile and envelope measurements are given as spatial resolution in the xy-plane (perpendicular to the beam), whereas the resolution for the Bragg peak measurements is given as spatial resolution in the z-direction along the beam. For the stack of SSBDs the uncertainty is given in MeV, because the author has given the uncertainty in energy [11]. For the beam flux measurements the range or order of magnitude for which the methods have been used is given. Moreover, when a method has been used by multiple authors, the best resolution has been used. Furthermore, from the table it can be seen that some methods have been shown more frequent in this literature study than others. That is because, except for some methods, the methods discussed in this literature study are quite standard.

2.2.6. Literature study discussion and conclusions

The goal of this literature study was to have a broad overview of the different techniques that are used for proton beam characterization. All the methods that have been described, the circumstances in which they have been used or modelled, and their accuracies, can help to choose the best approach to characterize the proton beam line in the experimental room of HollandPTC. Moreover, the results obtained in HollandPTC can be compared to the ones found in this literature study.

Table 2.2: Overview of methods found for beam characterization.

	Method	**Resolution**	**Used by**
Profile	Gafchromic film	<0.5 mm	[7, 21, 30, 36]
	Medipix2	55 μm	[7]
	PinPoint IC	0.5 mm	[36, 38]
	Scintillating screen	0.5 mm	[42]
	Solid state detector	1.63 μm	[32]
	Radio-fluorogenic gel	<0.1 mm	[47]
	Strip IC	1 mm	[42]
Envelope	Gafchromic film	<0.5 mm	[7, 21, 36]
	PinPoint IC	0.5 mm	[38]
	Medipix2	55 μm	[7]
	Scintillating screen	0.5 mm	[42]
Flux	FC	$10^5 - 10^9$ protons per second	[19, 26, 42]
	Integral chamber IC	$10^6 - 10^9$ protons per second	[42]
	Plastic scintillator	$10^1 - 10^5$ protons per second	[42]
	Medipix2	$10^0 - 10^9$ protons per second	[7]
Bragg peak	Multilayer IC	2 mm	[23, 42, 45]
	Stack of SSBDs	±0.14 MeV	[11]
	Water phantom + ICs	Depends on step size and size IC	[42, 43]
	SOI microdosimeter	10 μm	[45]
	Ionoacoustics	<0.1 mm	[3, 46]
	OSL films	Depends on spacing of films	[33]
	Plastic scintillator	0.25 mm	[2]
	Solid state detector	±7 μm	[32]
	Radio-fluorogenic gel	<0.1 mm	[47]

For the beam profile measurements, it is important to have a detector with a dimension large enough to get the entire profile including the halo of the beam. In this respect, Gafchromic films, a scintillating screen coupled with a CCD camera, radio-fluorogenic gel, or a multi-strip IC would be suited. Gafchromic films give an immediate idea of the beam dimensions, however, their analysis is more time consuming than a scintillating screen with a CCD camera where the image is directly available and digitized. On the other hand, in terms of spatial resolution, Gafchromic films and radio-fluorogenic gel would be the best option. A multi-strip IC and scintillating screen may have a lower spatial resolution, but with the standard software used for clinical quality assurance the digitized dose distributions can be acquired and then analyzed.

Flux measurements can be done with different methods depending on the intensity range. In the clinical range (>1nA) an FC, integral chamber IC, or Medipix2 could be used. For a lower range (<10^5 protons per second) a plastic scintillator or Medipix2 would be suited.

In the clinical environment Bragg peak measurements are performed with a water phantom and ICs, or with a stack of ICs (MLIC type). The water phantom measurements are definitely more accurate than MLIC measurements because they are performed directly in water. The SSBD method used in [11] or solid-state detector can only be used for low energy beams, resulting in being inapplicable for therapeutic proton beams. In this case, in fact, a thicker solid-state detector will be needed increasing the costs and the complexity of the readout system. The OSL film method of [33] is too imprecise for an exact position of the Bragg peak. Additionally, each film should be analyzed separately which would make it more time consuming than the other methods. Even though the SOI of [45] has a high resolution, the use of microdosimetry and an MKM would make it unnecessarily complex. The use of plastic scintillators would be an option for higher intensities, if the quenching effects can be overcome such as Archambault et al. [2] suggested. Ionoacoustics and radio-fluorogenic gel would be two possibilities when they can be used with a therapeutic beam and a standard procedure can be done.

All in all, it can be concluded that proton beam characterization methods are well studied in literature and some methods are widely used. Because of the challenges in proton therapy, such as an accurate range verification, in vivo dosimetry, or online dose monitoring new techniques with higher accuracy are being developed and studied.

The methods for the characterization that are used in this thesis have all been discussed in this literature study. The choice depended on the accuracy of the methods, the complexity of the methods, and the availability of the devices and materials at HollandPTC. The devices include several types of ICs, a scintillating screen, and an FC. In the next chapter the methods are explained more extensively.

3

Materials and Methods

Information about the experimental area, experimental setup, and materials that have been used for all experiments is given in the following sections. Furthermore, the experimental setup and the processing of the data is explained for each type of experiment separately. All data processing has been performed in MATLAB® version R2017a.

3.1. HPTC experimental room

As was shown in figure 3, the experimental room is the first room that gets served by the cyclotron. The room is equipped with a fixed horizontal beam line and the system can deliver single pencil beams with nominal energies that can be requested varying from 70 up to 240 MeV and nominal currents from 1 nA up to 800 nA. A schematic view is given in figure 3.1, which shows the beam line entering the room as the grey line, the isocenter marked by the crossing of the lasers in green, the area available for the experimental setup as the rectangle with black edges, and the beam dump at the end of the line in blue. Some dimensions are presented in the figure too. A picture taken from the experimental room is presented in figure 3.2, where almost all the elements shown in the schematic can be seen. In the next section the experimental setup of the experiments performed in this room will be presented.

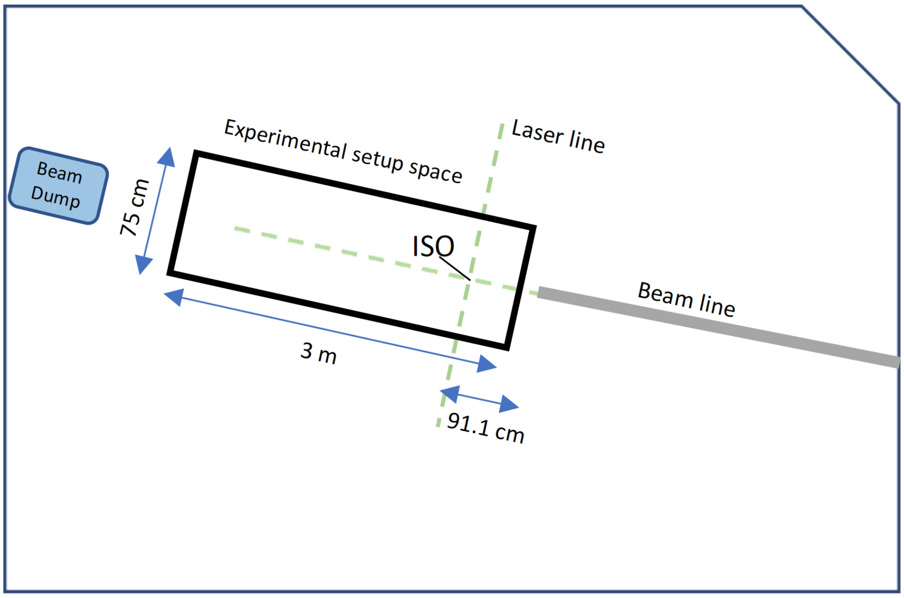

Figure 3.1: Schematic view of experimental room. Beam line in grey, lasers in green marking the isocenter, experimental setup space in the white rectangle with black edges, beam dump in blue. Image is not to scale.

Figure 3.2: Picture of experimental room. Courtesy of M.D.H. Rituerto Prieto

3.2. Experimental setup

For most of the experiments performed for this thesis the experimental setup is generally the same. This setup can be seen in figure 3.3. In this setup, a single pencil beam of a certain energy comes out of the exit window. A detector is placed (usually) at the isocenter, which is 91.1 cm from the exit window, and measures the characteristics of interest. At the end of the beam line the remaining protons lose their energy in the beam dump. The detector that will be used depends on the type of measurement that needs to be performed. In the next section the detectors that have been used for all the experiments will be discussed briefly.

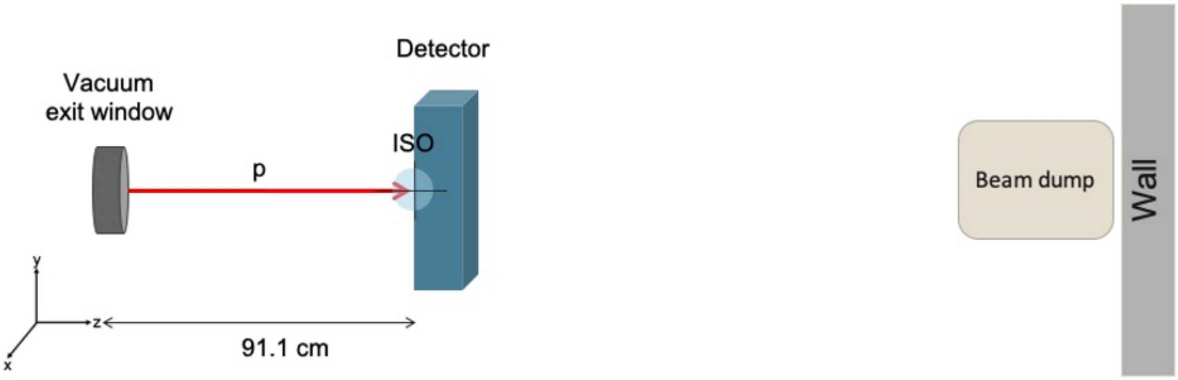

Figure 3.3: General experimental setup. Showing the proton beam coming out the exit window, a detector at the isocenter, and the beam dump and wall at the end of the line.

3.2.1. Detectors

For all the measurements that have been performed, several detectors have been used. All of them can be seen in figure 3.4 and are explained below.

NextQ

The NextQ, see figure 3.4A, is a medical device and can be used for QA and beam calibration. It is a multi strip ionization chamber manufactured by DE.TEC.TOR. The strip ionization chambers are in x- and y-direction with a sensitive area of 127 by 127 mm and can be used for beam profile- and positioning measurements along both dimensions with a spatial resolution of 1 mm. Additionally, the NextQ contains two integral chambers, which after calibration can be used for beam current measurements. The maximum sampling rate of the detector is 1 kHz. Measurements with the NextQ detector will thus give four outputs: a profile in x-direction,

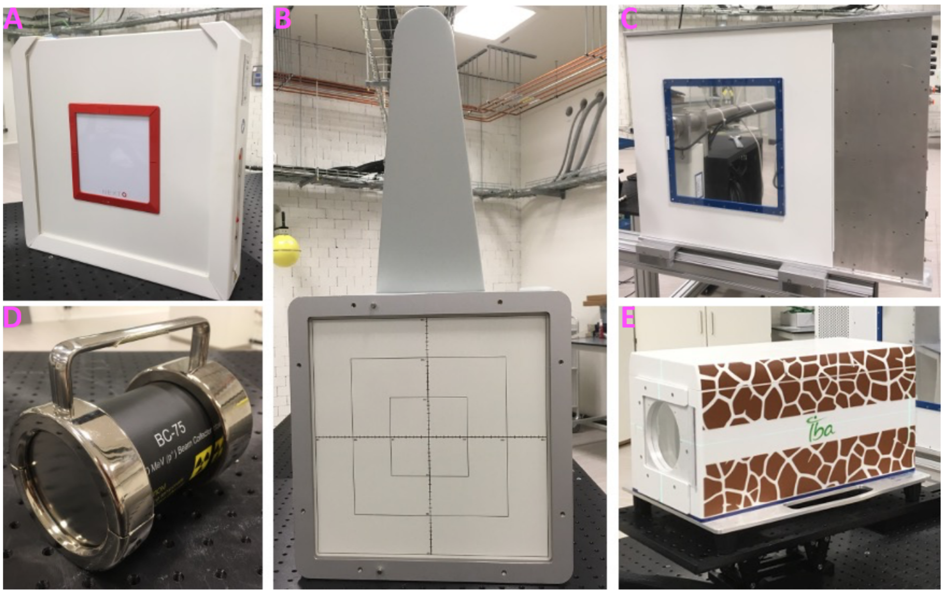

Figure 3.4: A) NextQ detector; B) Lynx detector; C) BM1 detector; D) Faraday Cup; E) Giraffe detector.

a profile in y-direction, and two raw number of counts, all of them as a function of time. The NextQ can be used to measure the beam profiles or spot sizes, and also for the beam current or total number of particles. The advantage of this device is that it can be put in between any setup and then can be used as a beam monitor to monitor the profile, position, and number of particles.

Lynx

The Lynx, figure 3.4B, is a detector by IBA Dosimetry. It consists of a scintillating screen coupled to a CCD camera and can be used for either QA or beam characterization. The sensitive area is 300 by 300 mm with a spatial resolution of 0.5 mm. One can choose to either make a single shot or a movie. The Lynx detector can be used to retrieve 2D images of a single pencil beam or a (passively scattered) field. In the case of a single pencil beam the images can be used for beam spot measurements, giving the full 2D beam spot of which also the profiles can be retrieved, where the NextQ only gives the profiles. The latter is an advantage that the Lynx has over the NextQ detector. Another advantage when doing beam profile measurements is the higher spatial resolution of the Lynx compared to the NextQ. The Lynx detector however is not transparent and should be placed as the final element of the setup.

BM1

The BM1, figure 3.4C, is a medical device by DE.TEC.TOR. It is a beam monitor ionization chamber with a sensitive area of 30 by 30 cm and contains two integral channels, both with a 1 millisecond resolution. The BM1 will give a raw number of counts as a function of time for both channels. Besides monitoring the beam, the BM1 can be used for beam current measurements once the detector is calibrated. The advantage over the NextQ is that the BM1 has got a larger sensitive area.

Faraday Cup

The BC-75 beam collector, figure 3.4D, is a Faraday Cup by Pyramid Technical Consultants. It is 75 mm in diameter (70.5 mm sensitive diameter) and can be used to count the number of protons (charge) for beam current measurements. The accuracy is better than 2% for energies from 70 MeV up to 240 MeV. The sampling rate or integration time goes up to 100 microseconds. As the Faraday Cup will stop all the protons, it should be placed as the final element of the experimental setup. Putting the Faraday Cup as close as possible to the exit window however will ensure that it will measure as much protons as possible because the beam will have less lateral spread than further away. Besides for beam characterization, the Faraday Cup can also be used for calibration of other detectors. This can for example be done for the integral channels of the NextQ and the BM1. The disadvantage of the FC compared to the BM1 for beam current measurements is the fact that the sensitive area of the FC is smaller than the sensitive area of the BM1. An advantage however is the higher sampling rate, which makes it possible to measure the beam current on a finer time structure.

Giraffe

The Giraffe, figure 3.4E, is an MLIC detector by IBA-Dosimetry. The Giraffe is used for Bragg Peak measurements and outputs full depth-dose curves and ranges. It consists of 180 parallel plates of water equivalent material with a 2 mm spacing and has a 1.879 mm water equivalent thickness resolution. The detector is suited for measuring beam energies up to 230 MeV. For higher energies the amount of plates is not sufficient to completely stop the beam. Besides depth-dose curves the Giraffe software returns the proton range in water with an accuracy of 0.5 mm.

3.2.2. Other beam line elements

Besides characterization of the single pencil beam, some other experiments have been performed. These were spread-out Bragg peak measurements and passive scattering measurements. Both experiments have their own setup, using different beam line elements. For the spread-out Bragg peak measurements, a ridge filter has been used which is designed and produced by GSI and can be seen in figure 3.5. This ridge filter is designed to give a spread-out Bragg peak of 2.5 mm for a beam energy of 150 MeV.

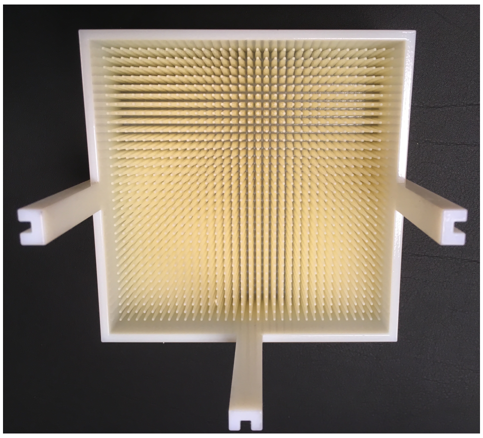

Figure 3.5: Ridge filter used for creating a spread-out Bragg peak. Designed for a beam energy of 150 MeV.

Passive scattering has been done by making use of a dual ring scattering system. This setup uses a single lead foil as the first scattering element and a dual ring consisting of a lead center and an aluminium outer ring. Both elements are designed to be used with a 150 MeV proton beam. Figure 3.6 shows both the lead foil and the dual ring.

Figure 3.6: A) Dual ring; B) Single scattering foil.

In the next sections all performed experiments are explained, together with how the detectors and beam line elements have been placed in the experimental setup. Additionally, the main steps of the data processing for each experiment are given.

3.3. Beam spot measurements

3.3.1. Experimental setup beam spot measurements

The experimental setup of the beam spot measurements is the same as the one shown in figure 3.3 with the NextQ detector placed at isocenter. A picture of the setup can be seen in figure 3.7. This setup will give beam profiles in both x- and y- direction. The measurements have been done for nominal energies of 70-240 MeV in steps of 10 MeV. The reason that this detector has been chosen to do the beam spot measurements is that at the time of the experiments we were not only interested in the beam profiles, but also in the raw number of counts, which could then be used to get the total number of protons or the beam current after a possible calibration later on.

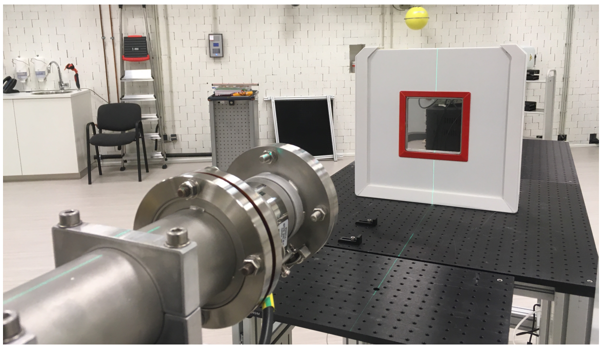

Figure 3.7: Picture of beam spot measurement setup with the NextQ detector placed at the isocenter.

3.3.2. Data processing beam spot size and full characterization

As is seen in literature [42], the beam spot size is given in terms of the standard deviation σ of a single Gaussian:

$$f\left(x,\mu,\sigma\right) = \frac{1}{\sqrt{2\pi}\sigma} e^{-\frac{(x-\mu)^2}{2\sigma^2}}, \tag{3.1}$$

with f being the profile in x- or y-direction, x in this case either the x- or y-vector, μ the mean position of the Gaussian and σ the standard deviation of the Gaussian. Additionally, the asymmetry of the beam spot is calculated by [42]:

$$AS\,(\%) = 100 \cdot \frac{\sigma_x - \left(\frac{\sigma_x+\sigma_y}{2}\right)}{\frac{\sigma_x+\sigma_y}{2}}, \tag{3.2}$$

with AS the asymmetry of the beam spot, σ_x the beam spot size in x- direction, and σ_y the beam spot size in y-direction. The NextQ detector software gives out two files after each measurement is saved. One file contains the data of the horizontal (x) profile and one of the integral channels in time, and the other one of the vertical (y) profile and the other integral channel. For characterization of the beam spot the data of the integral channels is not needed. This means that for data processing first the x- and y-profiles of the latest time stamp are extracted. The profiles can be fitted to the function given in equation 3.1 to obtain σ_x and σ_y. With equation 3.2 the asymmetry of the beam spot can be calculated. These steps are repeated for every measurement of every energy. The uncertainties of the determined beam spot size come from the detector resolution (1 mm) and from the uncertainty of the fit parameters.

Additionally to determining the beam spot size for all the energies (70-240 MeV), a full characterization for the beam spot at the isocenter has been done for one beam energy (70 MeV). This has been done to see if another distribution than the single Gaussian of equation 3.1 will have a better agreement with the measured data. As stated in section 2.2.1. Bellinzona et al. [4] have found that other distributions than a single Gaussian will improve the description of the tails of the measured beam spot. The method to do the full characterization is the same as for determining the beam spot size, only now fitting with a different function than the single Gaussian. It has been chosen to do this for two distributions: a double Gaussian and a Gauss-Rutherford, as they have been found to give similar results as more complex distributions, but at the same time will be less computationally expensive. The double Gaussian is given by:

$$f(x) = N\left\{(1-W)\frac{1}{\sqrt{2\pi}\sigma_1}e^{-\frac{(x-\mu)^2}{2\sigma_1^2}} + W\frac{1}{\sqrt{2\pi}\sigma_2}e^{-\frac{(x-\mu)^2}{2\sigma_2^2}}\right\}, \tag{3.3}$$

where again f is the beam profile in either x- or y-direction, x is the x- or y-vector, N is a normalization factor, W is the relative weight for each of the Gaussians, σ_1 and σ_2 the standard deviations of the two Gaussians, and μ the mean position of the Gaussians with the assumption that both have the same mean. The Gauss-Rutherford is given by:

$$f(x) = N\left\{(1-W)\frac{1}{\sqrt{2\pi}\sigma}e^{-\frac{(x-\mu)^2}{2\sigma^2}} + W\frac{2b^{3/2}}{\pi}\frac{1}{\left(y^2+b\right)^2}\right\}, \tag{3.4}$$

where f, x, N, W, σ, and μ are the same as for equation 3.3, and b represents the horizontal shift of the Rutherford-like component of equation 3.4.

3.4. Beam envelope measurements

3.4.1. Experimental setup beam envelope measurements

The experimental setup of the beam envelope measurements can be seen in figure 3.8. The setup it almost the same as the one seen in figure 3.3, with the difference being that the detector is placed at different distances from the exit window. This is because the beam spot size has to be measured as a function of distance in air from the exit window. The detector that has been used for this experiment is the Lynx detector and a picture of the setup for one of the measurements with the detector closer to the exit window is shown in figure 3.9. For the experiment the detector has been placed at seven different distances from the exit window for five different beam energies which are all listed in table 3.1 and table 3.2. Furthermore, in the Lynx software one can change two settings for each measurement: the iris and the measurement time, both of which should be appropriately chosen to avoid saturation of the image. The iris can vary from 0 to 100% and the exposure time can be set in milliseconds. Depending on the energy and nominal current of the requested beam, suited settings should be found. The nominal current, iris settings and exposure times used for the beam envelope measurements are given in Appendix A.

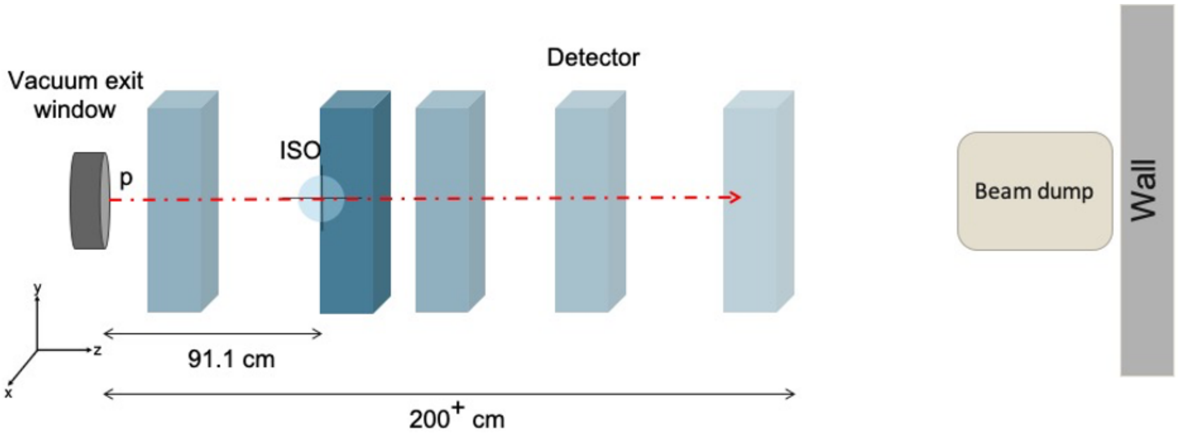

Figure 3.8: Experimental setup beam envelope measurements. The detector will be placed at different positions along the beam line to measure the beam spot size as a function of distance in air from the exit window.

3.4.2. Data processing beam envelope measurements

The lynx detector software produces a full 2D matrix of the beam spot, of which the profiles can be taken out in x- and y-direction. In a similar way as for the beam spot characterization, the profiles can be fitted to the Gaussian function of equation 3.1 to retrieve the beam spot size in x- and y-direction (σ_x and σ_y). Doing this for every energy and every distance, one can plot the beam spot size as a function of distance from the exit window for each beam energy. The uncertainties of the beam spot size for the beam envelope come from the detector resolution (0.5 mm) and the uncertainties in the parameters of the fit.

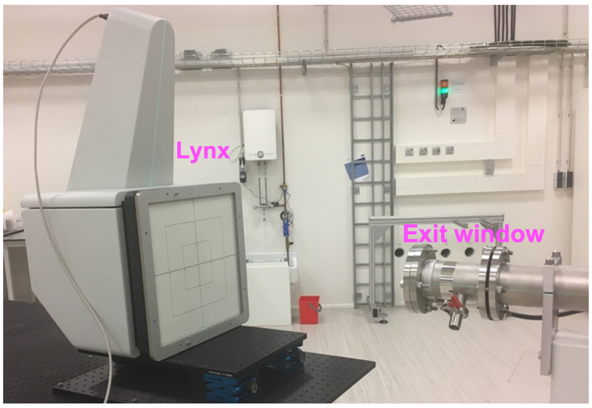

Figure 3.9: Picture of the experimental setup for the beam envelope measurements. The Lynx detector is positioned at one of the positions close to the exit window.

Table 3.1: Energies used for beam envelope measurements.

Energy (MeV)
70
120
150
200
240

Table 3.2: Distances used for beam envelope measurements

Distance (cm)
23
53
91.1 (ISO)
123
153
183
204.5

3.5. Beam current measurements

3.5.1. Experimental setup beam current measurements

The beam current measurements can be done in two ways. One of them is with the setup from figure 3.3, with the Faraday Cup placed at the isocenter. The other one is the same setup, but then together with the BM1, which is placed right after the exit window. The second setup can be used to measure the beam current and calibrate the BM1 with the help of the Faraday Cup at the same time and can be seen in figure 3.10. The setup of figure 3.10 is the one that finally has been chosen to use, with a picture of the setup shown in figure 3.11. The measurements have been done for nominal beam energies ranging from 70 up to 240 MeV. Once the BM1 is calibrated, it can be placed after the exit window for every experiment to use as a beam monitor to monitor the beam current or total number of protons.

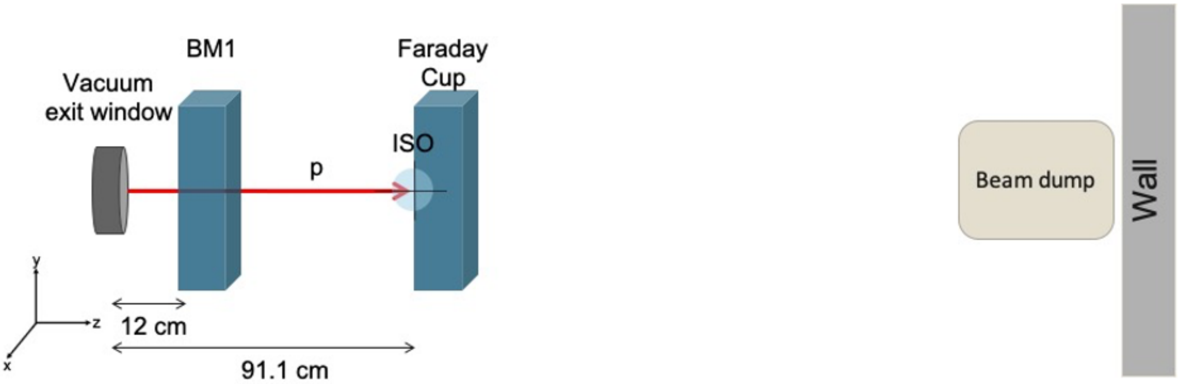

Figure 3.10: : Experimental setup for BM1 calibration. Showing the beam coming out the exit window, passing though the BM1 and getting collected in the Faraday Cup at the isocenter.

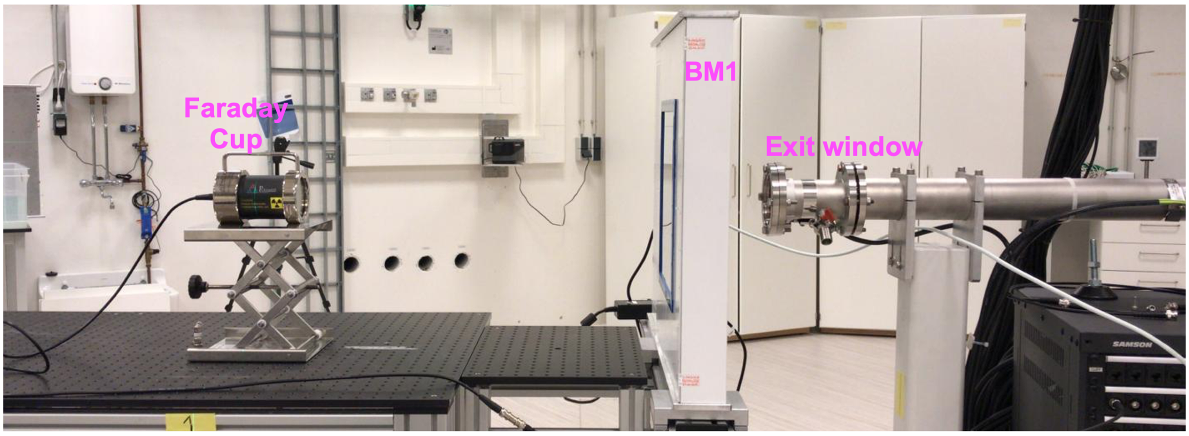

Figure 3.11: Picture experimental setup beam current measurements and BM1 calibration. With the Faraday Cup placed at the isocenter and the BM1 placed just after the exit window.

3.5.2. Data processing beam current measurements Faraday Cup

The Faraday Cup is a charge collector and provides how many Coulombs have been measured as a function of time. As current equals charge per time unit, the Faraday Cup can also provide the current that has been measured. The latter feature has been chosen for these experiments, which outputs the measured current as a function of time. In the data processing to determine the beam current for each measurement, the mean of the measurement points is taken to get the mean current. The Faraday Cup manual provides a gain for every energy, which can be used to correct all the measurements. After the correction, the transmission efficiency of the system can be retrieved by dividing the measured current by the nominal current. When the beam current is not of interest, but the number of protons, it is not necessary to first take the mean of the data points. Instead, after correcting for the gain, the measured current (in Amperes) can be integrated over the time and then divided by the elementary charge. The total number of measured protons will be needed for calibration of the BM1. Uncertainties in the measurements with the Faraday Cup mainly come from the standard deviation in the measured signal of which the mean value has been taken. The uncertainty of the measurements themselves are corrected for by the gain provided in the manual. The gain comes from two independent institutions that have performed measurements with the BC-75 beam collector.

3.5.3. BM1 calibration method

The BM1 as explained in section 3.2.1 contains two integral channels, which give a raw number of counts as a function of time. Taking the raw number of counts of the latest time stamp and comparing it to the number of protons that has been counted with the help of the Faraday Cup during the same measurement, a conversion factor for each of the integral channels can be obtained. This conversion factor will be different for every beam energy. By using the conversion factor, one can go from raw number of counts, given by the BM1, to the actual number of protons for each measurement. Since the BM1 gives the signal as a function of time, it is also possible to calculate the beam current with the help of the conversion factors. As the sampling rate is known (as set during the measurement) and the number of protons measured as a function of time is known, now by multiplying the number of protons with the elementary charge and then dividing by the time will give the beam current. For BM1 measurements the uncertainty comes from the statistical uncertainty in the raw counts, which is equal to the square root of the raw counts.

3.6. Bragg peak and spread-out Bragg peak measurements

3.6.1. Experimental setup Bragg peak measurements

The Bragg peak measurements are done with the same experimental setup as seen in figure 3.3, with the Giraffe detector placed at isocenter as in figure 3.12. The Bragg peak measurements have been done for nominal energies of 70 to 230 MeV in steps of 10 MeV. Initially it was intended to perform the measurements with another MLIC ionization chamber, the QUBE detector by DE.TEC.TOR. As the QUBE was not ready to be used at the time of the experiments yet, it was chosen to use the Giraffe detector which has been borrowed from the

Medical Physics department of HollandPTC. Future depth dose measurements however will be performed with the QUBE detector.

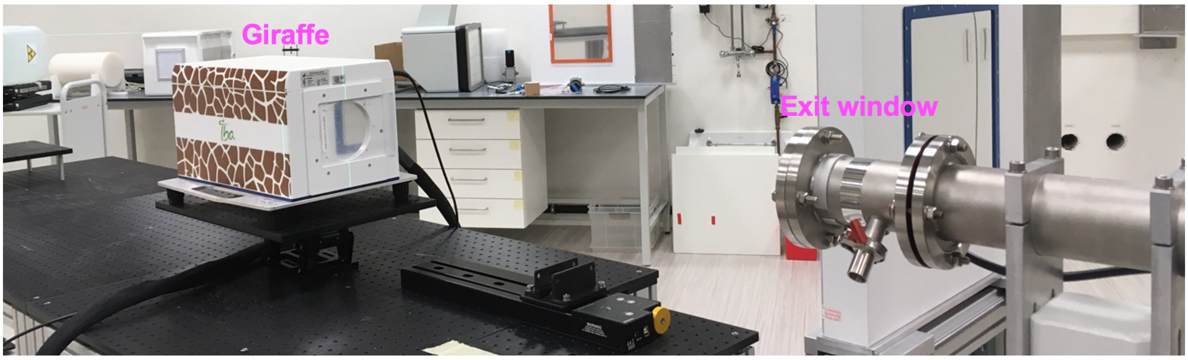

Figure 3.12: Picture of experimental setup for Bragg peak measurements. The Giraffe detector is placed at the isocenter.

3.6.2. Data processing beam energy

The Giraffe detector outputs several data that are of importance for each measurement. These are the d_{80} and d_{20} (both in water), and a file with the data of all the channels of the detector representing the Bragg curves. From the d_{80} one can obtain the beam energy at the isocenter by using the NIST data on proton range in liquid water [28]. The NIST data list the d_{80} in liquid water for proton energies ranging from 1 keV to 10 GeV. If one wants to know the energy of the beam before the exit window, one has to correct the d_{80} for the WET of the material (kapton) of the exit window, and the WET of the medium (air) between the exit window and the isocenter. For this correction, the WET is determined by equation 1.5. Adding the WET of the exit window and air to the d_{80} and d_{20}, the corrected d_{80} ($d_{80,corrected}$) and d_{20} ($d_{20,corrected}$) are obtained. From the $d_{80,corrected}$ the energy right before the exit window can be determined in the same way as from the d_{80} at the isocenter. In this way a comparison can be made between the nominal energy and the actual energy right before the exit window.

3.6.3. Experimental setup spread-out Bragg peak measurements

The setup of the spread-out Bragg peak measurements is the same as the Bragg peak measurements, but then with a ridge filter placed in between. A schematic of the setup is shown in figure 3.13 and a picture taken from the setup in figure 3.14. The SOBP measurements have been performed for 150 MeV, which is the energy that the ridge filter is designed for, and a couple of additional energies (100, 120, 180, 200 and 230 MeV). The measurements at other beam energies have been done to see if the ridge filter possibly can be used for other energies than 150 MeV too.

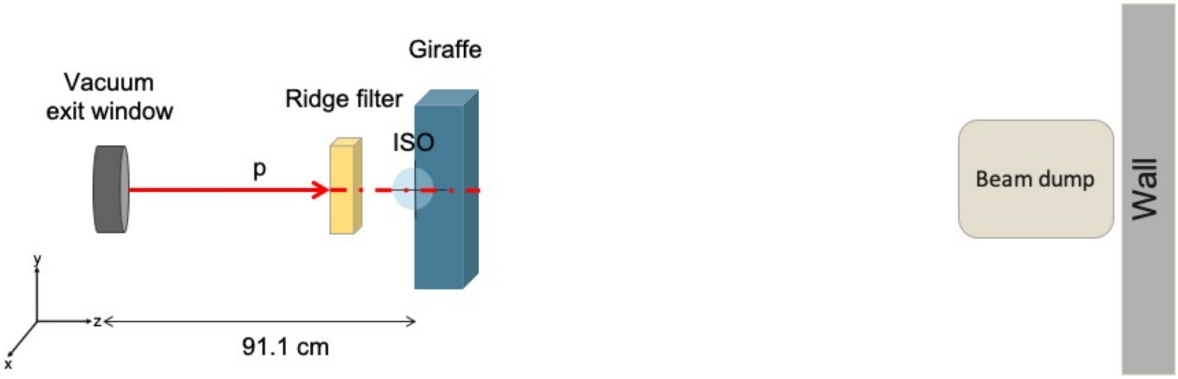

Figure 3.13: Schematic of experimental setup for SOBP measurements.

Figure 3.14: Picture of experimental setup for SOBP measurements. Ridge filter can be seen in front of the Giraffe detector.

3.6.4. Data processing spread-out Bragg peak

As mentioned in section 3.6.2 the Giraffe detector will give depth-dose curves for each measurement. In technical terms, the SOBP width is equal to the distance between the proximal 90% (p_{90}) and the distal 90% (d_{90}) and can be retrieved from those depth-dose curves [29]. In the data processing however, also bigger and smaller widths have been chosen and the uniformity in z-direction has been calculated for all of those widths. The uniformity is calculated by [43]:

$$U\,(\%) = 100 \cdot \left(1 - \frac{I_{max} - I_{min}}{I_{max} + I_{min}}\right), \tag{3.5}$$

with U the uniformity, I_{max} the maximum pixel intensity in the region of interest, and I_{min} the minimum pixel intensity in the region of interest. The aim is to have a uniformity of at least 98% over the SOBP region.

3.7. Passive scattering measurements

In these experiments the goal was to create a big field (diameter of at least 10 cm) with a uniformity of at least 97% by using a passive scattering setup.

3.7.1. Passive scattering experimental setup

The big field is created by using a single lead scattering foil and a dual ring, which were both shown in section 3.2.2. An image of the intensity of the field is then made with the Lynx detector. The experimental setup can be seen in figure 3.15 and a picture of part of the setup can be seen in figure 3.16. Since the BM1 is going to be placed after the exit window permanently to monitor the beam in future experiments, in the passive scattering experiments it has been chosen to put it in place at that same position. This will improve the reproducibility of the field in the future. Different distances between the exit window, foil, dual ring, and Lynx detector have been chosen by means of trial and error to see which combination of distances gives the biggest field with the highest uniformity. The distance between the Lynx detector and the exit window will have an impact on the dose rate. In the case of a smaller distance the advantage is that the dose rate of the field (per unit area) is higher, but the drawback is the limitation of the field size. Placing the Lynx at a larger distance will allow for bigger field sizes, only due to the divergence of the field the dose rate will reduce.

3.7.2. Data processing passive scattering

The Lynx detector will provide a 2D matrix of the measured field. For circular areas with radii of 3, 5, 8, 10, and 12.5 cm with the origin at the center of the image, the uniformity has been calculated by equation 3.5. The same has been done for square areas with sides of 6, 10, and 16, 20, and 25 cm with the origin of the square at the center of the image. An example can be seen in figure 3.17, where an arbitrary field is drawn, with a circular area in red and a square area in green for which the uniformities would then be calculated. In future experiments a collimator will be put behind the dual ring to collimate the field. Since at the time of these experiments it was yet to be decided whether the collimator would be circular or square, the uniformity is calculated for both shapes.

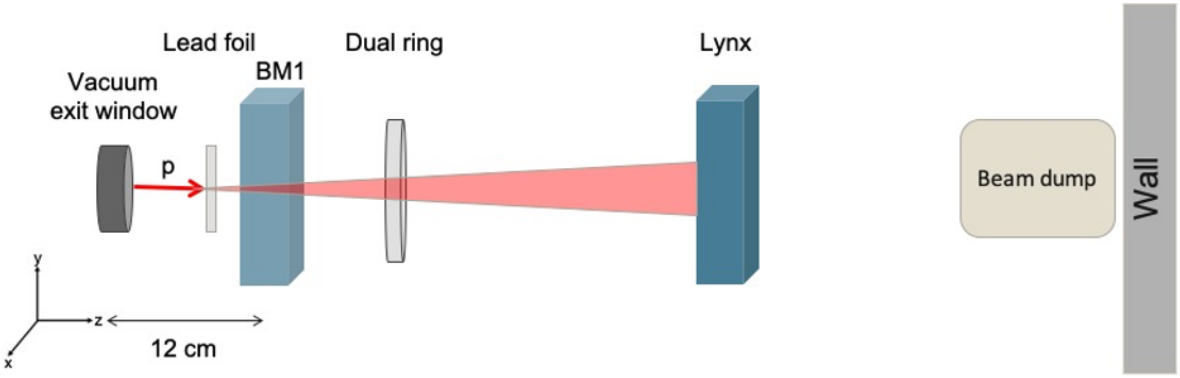

Figure 3.15: Experimental setup for passive scattering. The proton beam gets scattered in the lead foil, passes though the beam monitor, gets scattered in the dual ring, and the field is detected by the Lynx. The optimal distances between the lead foil, dual ring, and lynx detector are yet to be determined during the experiments.

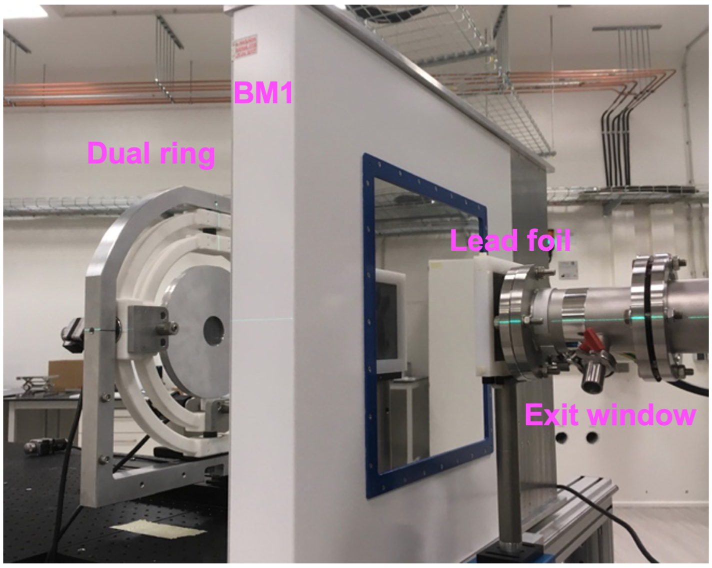

Figure 3.16: Part of passive scattering experimental setup, showing the exit window, lead foil, BM1, and dual ring.

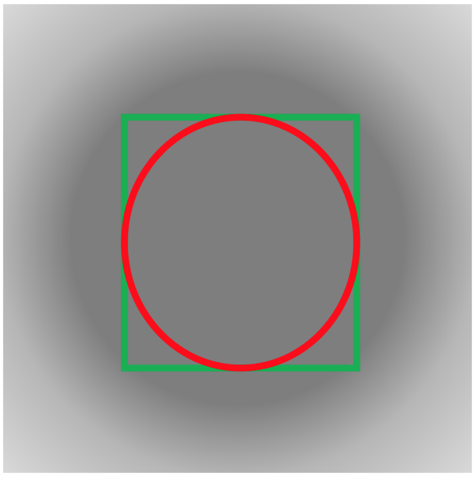

Figure 3.17: Arbitrary field with a circular area and square area for which the uniformity would be calculated.

4

Results and Discussion

In this chapter the results of the beam characterization are presented and discussed. Relevant images are shown, and some results are presented in tables.

4.1. Beam spot isocenter

In figure 4.1 the normalized beam profiles in x-direction for five different energies (70, 100, 160, and 240 MeV) at the isocenter are shown on top of each other, measured with the NextQ detector. This is done to visualize the changes in the profile as the energy of the beam is higher or lower. First of all, it can be seen that the profiles are of Gaussian shape as expected. Secondly the figure shows very clearly that the higher the beam energy, the narrower the profile.

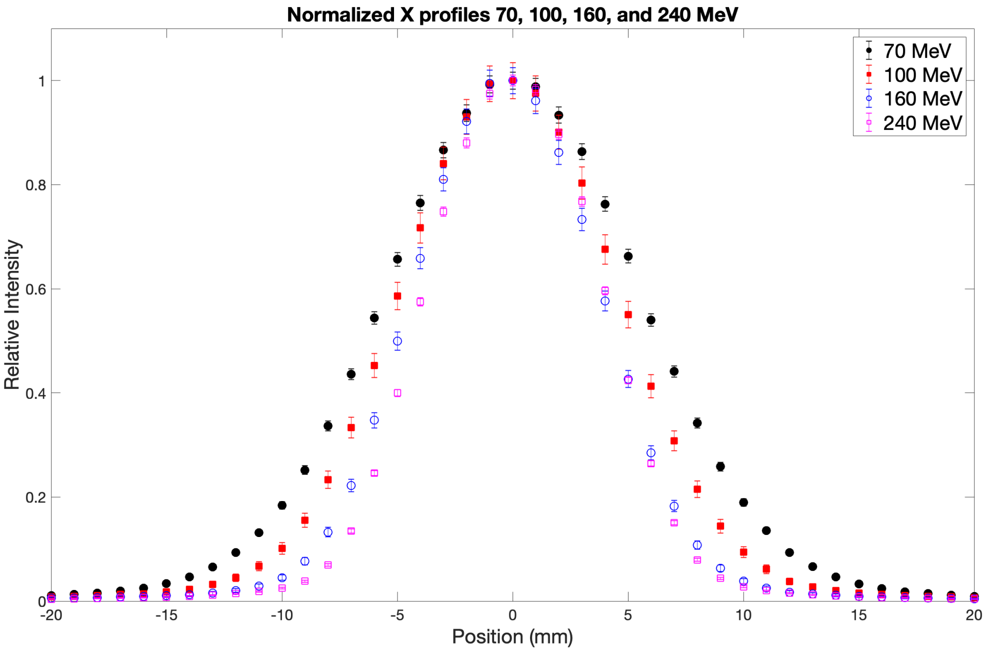

Figure 4.1: Normalized beam profiles at the isocenter in x-direction from 70, 100, 160, and 240 MeV single pencil beams measured with the NextQ (1 mm spatial resolution) detector. On the x-axis the position on the detector is shown and, on the y-axis the relative intensity. The error bars give the statistical uncertainty of the raw counts.

4.1.1. Beam spot size

Figure 4.2 shows the beam profiles of the 70 MeV single pencil beam at the isocenter in x- and y-direction along with the plots of the Gaussian fit from equation 3.1 for both profiles. Figure 4.3 shows the same, but then for 240 MeV.

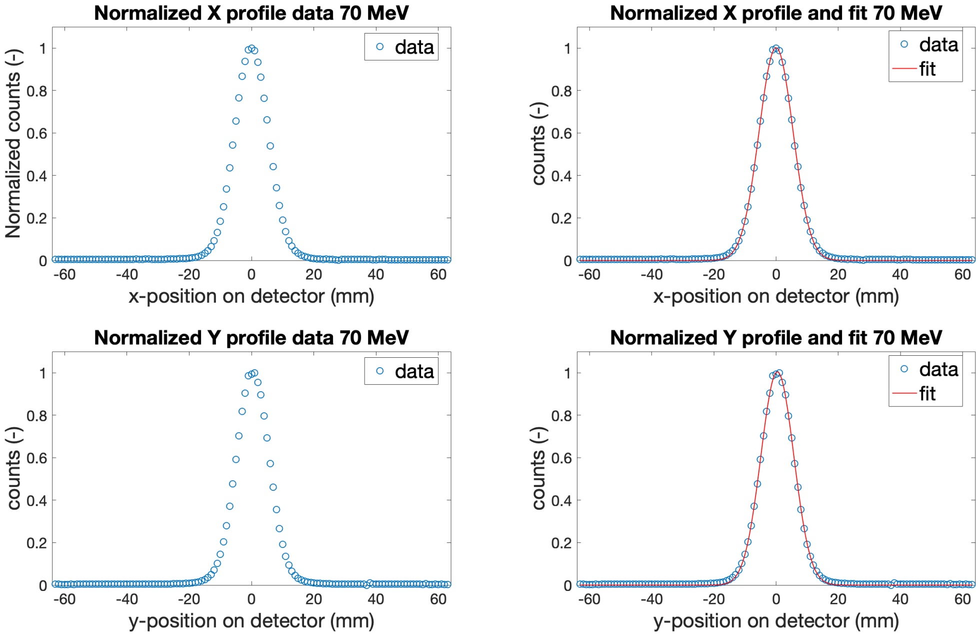

Figure 4.2: On the left normalized beam profiles in x- and y-direction measured at the isocenter for a 70 MeV single pencil beam and on the right shown together with a Gaussian fit. The uncertainties of the counts are not plotted as they fall within the data points.

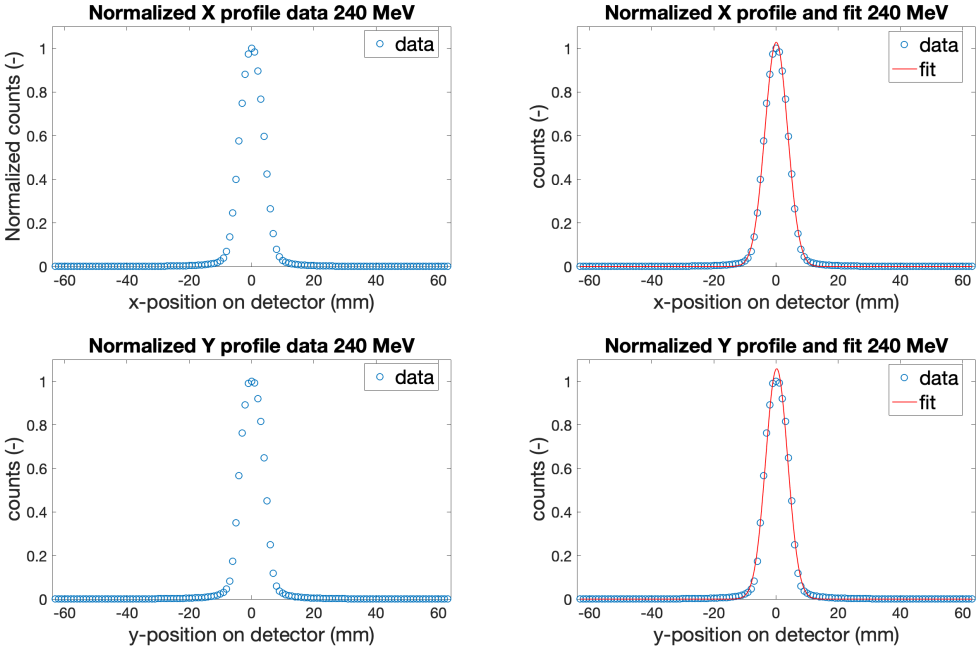

Figure 4.3: On the left normalized beam profiles in x- and y-direction measured at the isocenter for a 240 MeV single pencil beam and on the right shown together with a Gaussian fit. The uncertainties of the counts are not plotted as they fall within the data points.

From the figures it can be observed that the profiles are broader for 240 MeV than for 70 MeV, as was also seen in figure 4.1. Figure 4.2 shows that the Gaussian fit seems to agree with the profiles in both x- and y-direction, whereas figure 4.3 shows that for the y-profile the Gaussian fit does not agree at the top of the profile. This means that the profile in the x-direction is more Gaussian of shape at the isocenter than in the y-direction. The difference between the two energies can be explained by the fact that a 70 MeV beam has undergone more MCS and at bigger angles as explained in section 1.1.1, resulting in the profile being closer to a Gaussian. The difference between the x- profile and y-profile at 240 MeV can be a result of the ion optics being more visible in the y-profile at the isocenter.

The resulting σ_x and σ_y from the Gaussian fit for all of the energies are presented in table 4.1. Additionally, in this table the uncertainties ($u_{\sigma x}$ and $u_{\sigma y}$) of these parameters can be found, which are the uncertainties that come from the fit together with the uncertainty due to the detector resolution. It is seen that the biggest part of the uncertainty is caused by the spatial resolution of the detector (±0.5 mm). In the before-last column of table 4.1 the spot asymmetry (AS) as calculated by equation 3.2 is shown. When the asymmetry is equal to 0%, it means that the beam spot is circular in shape and otherwise it means that the beam spot has an elliptical shape, with the long axis along x if the asymmetry is positive and the long axis along y if the asymmetry is negative. Finally, the uncertainty of the calculated asymmetry (μ_{AS}) is given in the last column of table 4.1. This μ_{AS} comes from the propagation of the uncertainty of the beam spot sizes.

Table 4.1: Beam spot sizes σ_x and σ_y, and their uncertainties $u_{\sigma x}$ and $u_{\sigma y}$ for beam energies E together with the asymmetry AS and the absolute uncertainty of the asymmetry u_{AS} from the resulting fit for every energy at the isocenter.

E (MeV)	σ_x (mm)	$\pm u_{\sigma x}$ (mm)	σ_y (mm)	$\pm u_{\sigma y}$ (mm)	AS (%)	$\pm u_{AS}$ (%)
70	5.47	0.514	5.29	0.515	1.6	9.6
80	5.10	0.510	4.93	0.511	1.6	10.2
90	4.83	0.510	4.67	0.511	1.7	10.7
100	4.64	0.514	4.50	0.514	1.5	11.2
110	4.47	0.516	4.36	0.517	1.2	11.7
120	4.30	0.508	4.23	0.513	0.8	12.0
130	4.19	0.512	4.15	0.517	0.5	12.3
140	4.10	0.513	4.12	0.512	-0.2	12.6
150	4.02	0.511	4.04	0.520	-0.3	12.8
160	3.95	0.511	3.95	0.521	0.0	13.1
170	3.91	0.512	3.94	0.523	-0.5	13.2
180	3.86	0.511	3.90	0.524	-0.4	13.3
190	3.83	0.512	3.86	0.526	-0.4	13.5
200	3.80	0.512	3.81	0.527	-0.1	13.7
210	3.75	0.512	3.75	0.528	0.0	13.9
220	3.72	0.513	3.70	0.529	0.3	14.1
230	3.69	0.514	3.63	0.530	0.7	14.3
240	3.66	0.515	3.54	0.529	1.6	14.5

A plot of the beam spot sizes including error bars for all beam energies is shown in figure 4.4, where the beam spot size in x-direction is shown in red, and in y-direction in blue. From figure 4.4 it can be seen that the beam spot becomes smaller in both directions as the energy increases. This is what also could be seen from figure 4.1 and is explained by the beam undergoing more interactions in the energy selection system and other beam line elements in between the cyclotron extraction and the exit window for lower energies and thus becoming broader. Additionally, the protons undergo more multiple coulomb scattering at larger angles in the air between the exit window and isocenter when the energy of the particles is lower. These two effects together result in the trend of the beam spot sizes in figure 4.4. It can also explain that in between the lower energies (70 - 120 MeV) the decline in beam spot size is steeper. In figure 4.4 the asymmetry of the beam spot becomes visible too. The 0.0% asymmetry for the 160 MeV beam from table 4.1 can for example be traced back to the x and y spot sizes overlapping at 160 MeV in figure 4.4. Another aspect that catches the eye is that the uncertainties of the spot sizes as seen in table 4.1 and figure 4.4 seem rather big (up to about ±15% of the spot size). To reduce the uncertainty to roughly half this value, for future beam spot characterizations the Lynx detector can be used instead of the NextQ detector, since the spatial resolution of the Lynx is twice as small.

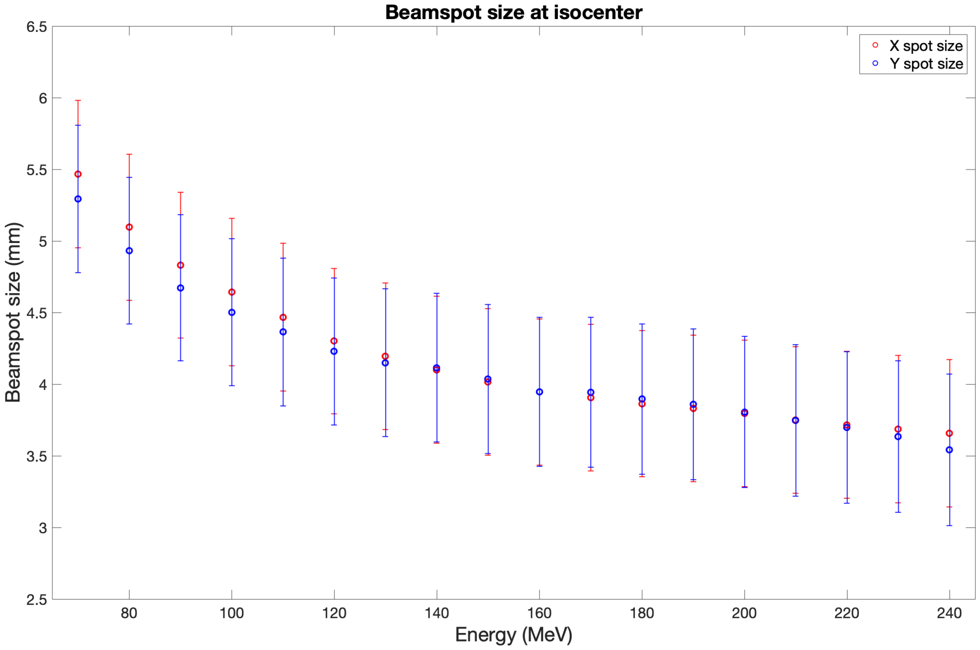

Figure 4.4: Beam spot size at the isocenter for 70 – 240 MeV in x- and y-direction (σ_x and σ_y) in red and blue respectively with error bars.

4.1.2. Characterization of the tails

A single Gaussian is not the best function to fit the profiles to, but in this case, it is only used to characterize the beam spot size. From figure 4.2 it seems that a single Gaussian describes the profiles quite well. Figure 4.5 however contains the same profiles together with the Gaussian fit on a logarithmic scale. In this figure it clearly shows that the single Gaussian does not agree with the data points of the beam profiles in the tail regions. What stands out are the sudden drop in counts just before 30 mm in the x-profile and the increase in counts just before 40 mm in the y-profile. This has been observed for multiple measurements, meaning that it is probably due to the gain of the detector channel being different or the channel being more sensitive to noise. The results of using equation 3.3 and equation 3.4 to fit the data to are shown in figure 4.6 and figure 4.7 respectively. It can be seen that both the double Gaussian and Gauss-Rutherford describe the tails of the profiles better than a single Gaussian. Table 4.2 provides the resulting parameters of the single Gaussian fit and the double Gaussian fit together with the sum of the squared error (SSE) for each of the fits. Table 4.3 contains the parameters for the Gauss-Rutherford. First of all by only looking at the figures it can be concluded that both a double Gaussian and Gauss-Rutherford give a better description of the beam profiles in the tail regions. From the SSEs in table 4.2 and table 4.3 it can be seen that this is not only qualitatively but also quantitatively true. With a double Gaussian the SSE reduces with 86% for the x-profile and 81% for the y-profile. For a Gauss-Rutherford the SSE reduces with 87% and 83% for the x- and y-profile respectively.

Table 4.2: Comparison between a single Gaussian and a Double Gaussian to describe the beam profile in x and y for a 70 MeV beam at the isocenter. σ_x and σ_y are given for the single Gaussian, together with σ_{x1}, σ_{x2}, σ_{y1}, and σ_{y2} for a double Gaussian. The SSE is given for the fits of the x- and the y-profiles.

Single Gaussian				Double Gaussian					
σ_x (mm)	SSE$_x$ ($\cdot 10^{-3}$)	σ_y (mm)	SSE$_y$ ($\cdot 10^{-3}$)	σ_{x1} (mm)	σ_{x2} (mm)	SSE$_x$ ($\cdot 10^{-4}$)	σ_{y1} (mm)	σ_{y2} (mm)	SSE$_y$ ($\cdot 10^{-4}$)
5.47	4.06	5.29	4.43	5.40	37.7	5.80	5.22	35.1	8.29

Table 4.3: Comparison between a single Gaussian and a Gauss-Rutherford to describe the beam profile in x and y for a 70 MeV beam at the isocenter. σ_x and σ_y are given for the single Gaussian, together with σ_x, σ_y, b_x, and b_x for a Gauss-Rutherford. The SSE is given for the fits of the x- and the y-profiles.

Single Gaussian				Gauss-Rutherford					
σ_x (mm)	SSE_x ($\cdot 10^{-3}$)	σ_y (mm)	SSE_y ($\cdot 10^{-3}$)	σ_x (mm)	b_x (mm)	SSE_x ($\cdot 10^{-4}$)	σ_y (mm)	b_y (mm)	SSE_y ($\cdot 10^{-4}$)
5.47	4.06	5.29	4.43	5.388	3369	5.39	5.21	2765	7.72

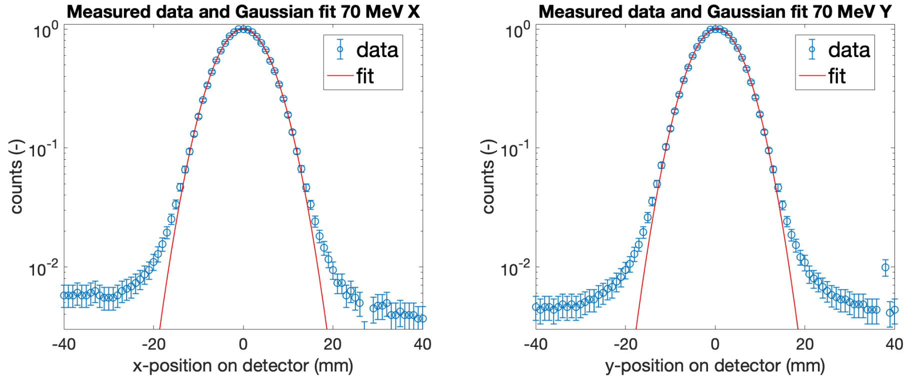

Figure 4.5: Beam profile at the isocenter for 70 MeV left in x-direction and right in y-direction with error bars and single Gaussian fit on a logarithmic scale.

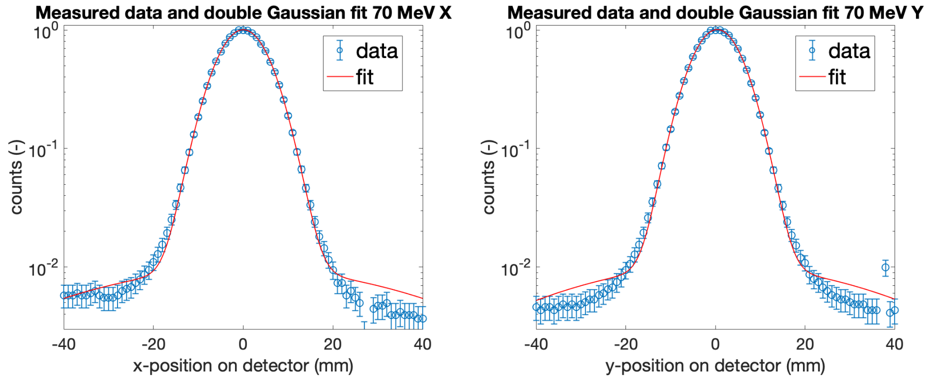

Figure 4.6: Beam profile at the isocenter for 70 MeV left in x-direction and right in y-direction with error bars and double Gaussian fit on a logarithmic scale.

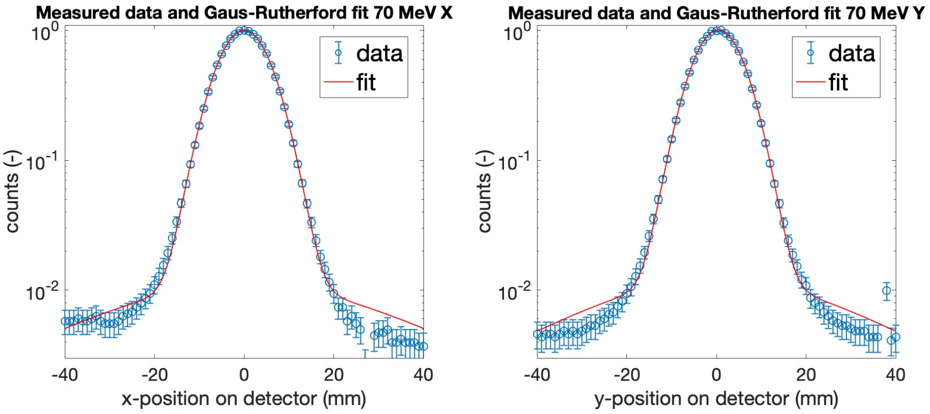

Figure 4.7: Beam profile at the isocenter for 70 MeV left in x-direction and right in y-direction with error bars and Gauss-Rutherford fit on a logarithmic scale.

4.2. Beam envelope

The beam envelope results for the five beam energies of table 3.1 are presented in figure 4.8. The beam spot size in x and y is shown as a function of distance in air from the exit window. The uncertainties in the beam spot sizes for these measurements are mainly caused by the detector resolution of 0.5 mm (±0.25 mm). From the figures it shows that the beam is a diverging beam, with the focus point right after the exit window. Also the beam spot becomes larger as the protons travel further away from the exit window, as along their path they undergo more MCS. The differences in beam spot size in between the energies becomes visible when comparing the figures to each other. An example is the beam spot size for 70 MeV at about 2 m distance from the exit window compared to the one for 240 MeV.

At the first couple distances from the exit window in the figures the ion optics of the system are clearly visible. The beam spot size in y is smaller in the beginning, meaning that the final focusing step of the beam happens in the y-direction. Furthermore the ion optics have been chosen such that at the third (ISO) and sometimes fourth position the beam spot is the most symmetric. After this point the scattering of the protons in air is the main contributor for the shape of the beam spot. What also can be seen is that the divergence of the beam, meaning the broadening of the beam spot over distance, is stronger in y-direction than in x-direction.

Some of the results of the beam envelope measurements can also be used for another purpose. The beam spot sizes measured at the isocenter during these experiments, can be compared to previously measured beam spot sizes obtained in section 4.1. Figure 4.9 shows the beam spot sizes measured at the isocenter with the NextQ previously, together with the beam spot sizes measured at the isocenter with the Lynx during the beam envelope measurements. From the figures it can be seen that the beam spot sizes measurements with the Lynx and NextQ at the isocenter agree within the uncertainties. The agreement is within 6% in x and 3% in y.

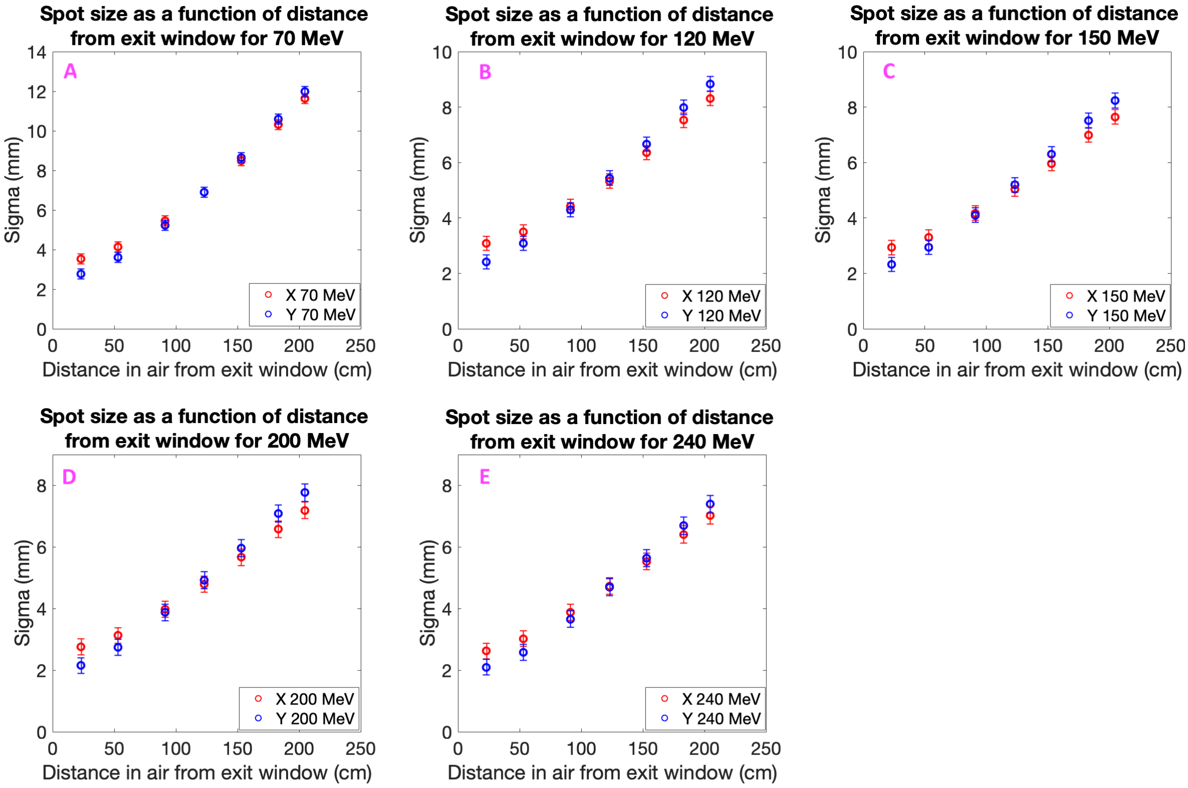

Figure 4.8: Beam envelopes for single pencil beams with energies of A) 70 MeV, B) 120 MeV, C) 150 MeV, D) 200 MeV, and E) 240 MeV. On the x-axis the distance in air from the exit window is shown in cm and on the y-axis the beam spot size sigma in mm. The red dots correspond to the spot size in x-direction and the blue dots to the spot size in y-direction.

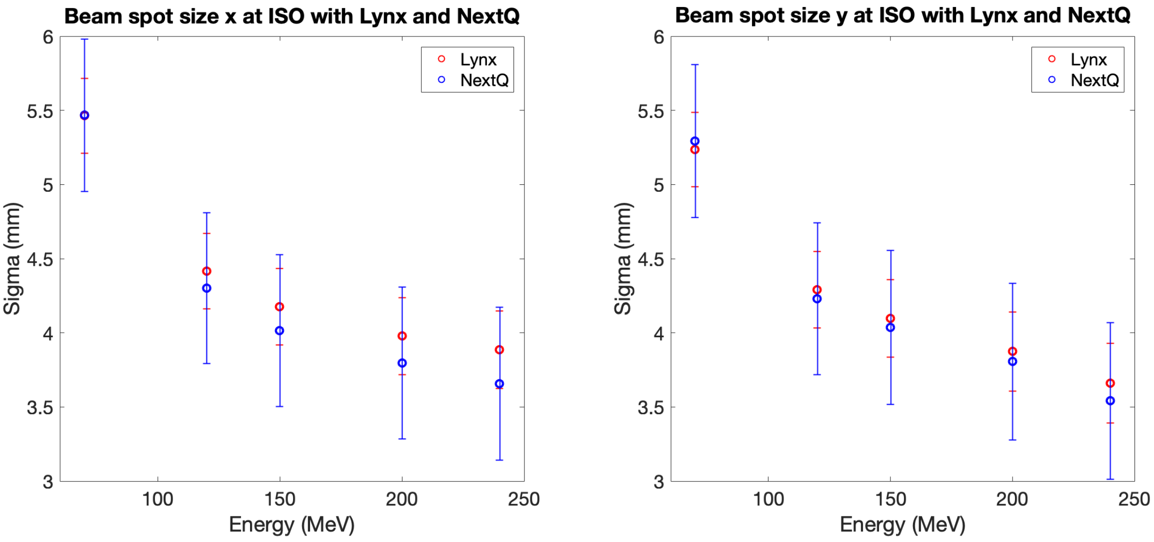

Figure 4.9: Beam spot sizes measured at the ISO centre with the Lynx detector compared to the beam spot sizes measured with the NextQ in x-direction (left) and y-direction (right). On the x-axis the beam energy is given in MeV, and on the y-axis the beam spot size sigma in mm together with the uncertainties.

4.3. Beam current and transmission efficiency

4.3.1. Transmission efficiency

For the beam current measurements, the most important characteristic is the transmission efficiency. Due to the beam line elements that the protons encounter in between the cyclotron extraction and the exit window there will be a difference between nominal current (the current at cyclotron extraction) and the effective current (the current at the isocenter). The lower the beam energy, the more material there will be to scatter and absorb the protons in the degrader and the energy selection system. This means that for lower beam energies the transmission efficiency will be less than for higher beam energies. The results of the beam current measurements are presented in table 4.4. In the first column the Energy of the beam is given in MeV. In the second column the number of protons measured per second at the isocenter for every nA nominal current is given. The before-last column shows the transmission efficiency, which is the current that is measured as a percentage of the nominal current. The final column gives the absolute uncertainty of the transmission efficiency. The transmission efficiency is also shown in figure 4.10. From results it can be seen that the transmission efficiency is increasing as the beam energy is increasing up, which was as expected as for higher energies less protons would be absorbed. The figure shows that the transmission efficiency seems to behave exponentially with increasing energy. The transmission efficiency overall is quite low, especially for lower beam energies, but this is not uncommon [42]. It does mean that it will be difficult to get high beam currents at target during experiments if lower energies are used. The maximum effective beam current that will be achievable, will be in the case of the highest energy (240 MeV) and the highest possible nominal current (800 nA). This will result in an effective beam current of about 45 nA at the isocenter. For a beam energy of 70 MeV and nominal current of 800 nA, an effective beam current of about 0.3 nA would be achievable.

The beam current measurements have been performed twice in the R&D bunker. After the first time we have become more familiar with the setup and gained knowledge on which measurement settings worked best. In figure 4.11 the results of the first beam current measurements can be seen together with the results that have been presented in figure 4.10. The experiments have been repeated several times for some beam energies. The blue data points are presented larger to be able to see them clearly. The blue data already are an average over several measurements. For the red data points all the measurements are shown separately to show what the experiment has taught us. What can be seen in the data from the previous experiment is that it seems to follow different curves. This means that in roughly half of the measurements, the measured beam current was probably lower than the actual beam current. All the points from the lower curve were measured at lower range settings (e.g. 1 nA) of the FC. It can be however that the beam current at the isocenter exceeds this range, depending on the nominal current and the transmission efficiency. The results of the experiment gave the insight that the range of the FC should not be set too low.

Table 4.4: Results beam current measurement. Showing the effective number of protons per second at the isocenter for every 1 nA nominal current, the transmission efficiency, and the absolute uncertainty of the transmission efficiency.

E (MeV)	p/s for 1 nA nominal ($\cdot 10^6$)	Transmission efficiency (%)	$\pm u_{transmission\ efficiency}$ ($\cdot 10^{-3}$ %)
70	2.57	0.0411	1.51
90	4.68	0.0749	2.33
100	7.15	0.115	2.95
120	9.19	0.147	3.98
150	18.6	0.297	7.95
180	40.2	0.644	12.7
200	71.1	1.14	49.3
220	118	1.89	26.7
240	349	5.60	134

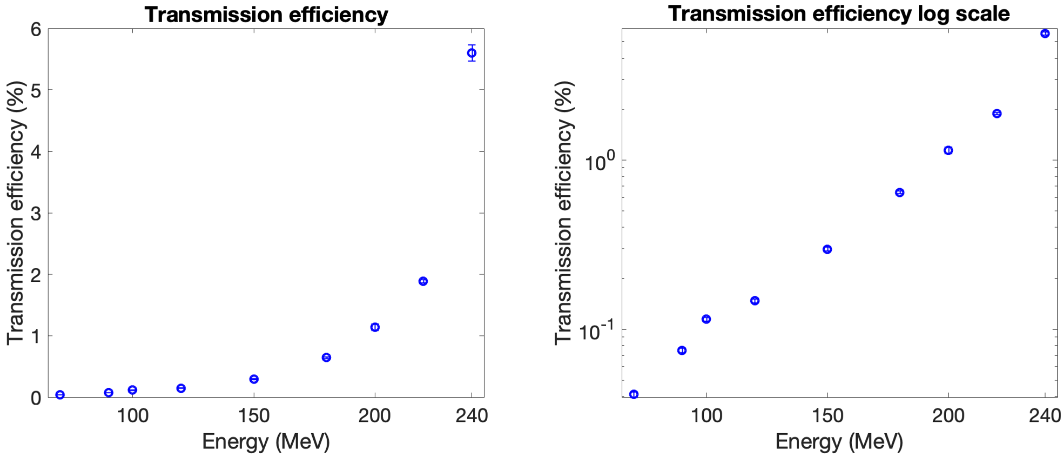

Figure 4.10: Transmission efficiency of the beam line. On the x-axis the beam energy is given in MeV, and on the y-axis the transmission efficiency in %. The left graph is plotted on a linear scale. In the right graph the y-axis is on a logarithmic scale.

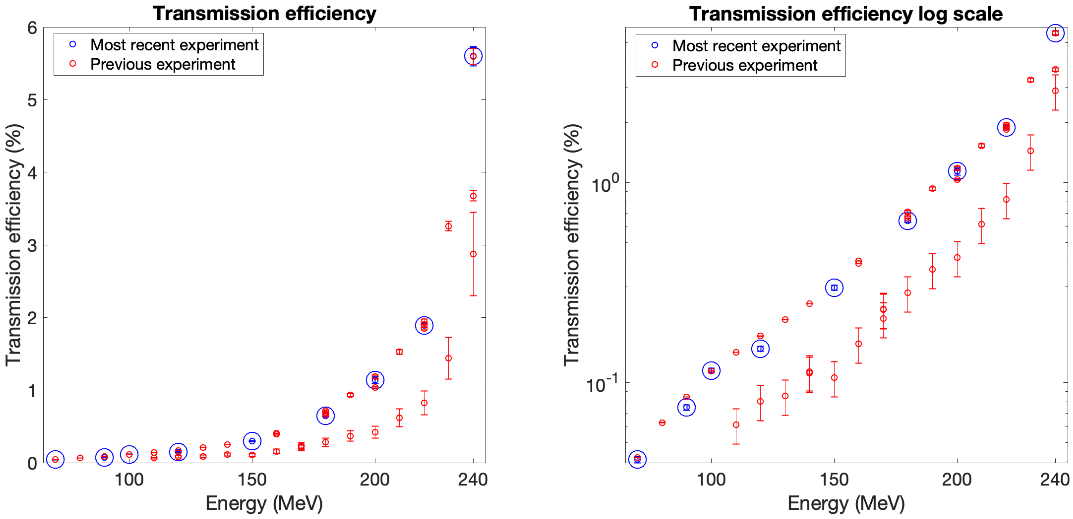

Figure 4.11: Transmission efficiency measured in recent and previous experiments. On the x-axis the beam energy is given in MeV, and on the y-axis the transmission efficiency in %. The left graph is plotted on a linear scale. In the right graph the y-axis is on a logarithmic scale.

4.3.2. BM1 calibration

For the BM1 calibration a comparison will be made between the conversion factors for the integral channels that have been found during the final experiments and the conversion factors that were found during a previous experiment. The latter conversion factors have been provided by M.D.H. Rituerto Prieto (personal communication, February 28, 2020). In table 4.5 the conversion factors are given that were found previously. Table 4.6 contains the conversion factors that were found later on during the final experiments of which the results of the Faraday Cup have been given in section 4.3.1 above. From table 4.5 and table 4.6 it can be seen that there is quite a difference in the uncertainty of the conversion factors between the experiments. This is explained due to the fact that the uncertainty comes from the statistical counting error. During the experiment of table 4.5 either the beam currents were higher or the measurements were taken during a broader time window. This means that the raw number of counts were higher resulting in a bigger statistical uncertainty of the counts.

Table 4.5: Conversion factors for the BM1 integral channels computed by M.D.H. Rituerto Prieto (personal communication, February 28, 2020).

Energy (MeV)	Conversion Ch.1 ($\cdot 10^3$)	Conversion Ch.2 ($\cdot 10^3$)	$\pm u_{conversion\ Ch.1}$	$\pm u_{conversion\ Ch.2}$
70	7.95	7.55	8.22	7.61
80	8.95	8.52	9.26	8.60
90	9.76	9.32	10.1	9.41
100	10.5	10.1	10.9	10.2
120	11.8	11.4	12.2	11.5
140	13.6	13.1	14.1	13.2
160	14.9	14.3	15.4	14.5
180	16.0	15.5	16.6	15.7
200	17.0	16.4	17.5	16.6
220	18.0	17.4	18.6	17.7
240	19.5	18.9	20.1	19.1

Table 4.6: Conversion factors for the BM1 integral channels computed during final experiments.

Energy (MeV)	Conversion Ch.1 ($\cdot 10^3$)	Conversion Ch.2 ($\cdot 10^3$)	$\pm u_{conversion\ Ch.1}$	$\pm u_{conversion\ Ch.2}$
70	7.16	7.53	6.33	6.82
90	9.16	9.58	6.78	7.26
100	9.98	10.4	6.55	7.01
120	11.2	11.7	6.96	7.42
150	13.2	13.8	6.08	6.45
180	14.9	15.5	5.02	5.31
200	16.0	16.6	4.25	4.50
220	17.2	17.9	3.62	3.83
240	19.1	19.8	2.52	2.66

Figure 4.12 shows a comparison between the conversion factors given in the two tables. What can be seen from the figure is that the conversion factor goes up as the beam energy increases. This can be explained by the fact that protons with higher energies will lead to less ionizations in the chamber than lower energy protons. For the same number of protons that pass though the chamber it means that the raw number of counts will be lower for higher beam energies, resulting in higher conversion factors needed. The figure showing the results for the first integral channel shows that the recent calibration gives a curve that lies lower than the previous one. For the second integral channel both curves are agreeing more. One would expect however that the curves for the second integral channel would show a difference more similar to the difference between the curves from the first integral channel, or the other way around. As the measurements have been done two months apart (January 2020 against March 2020) it could be that in the mean time the detector could have undergone maintenance, resulting in a change of the gain of one of the channels. To be sure if the difference is coincidental more experiments can be performed to see if the curves will agree more. Furthermore, for the

robustness it would also be better to repeat the measurements multiple times, to get more certainty on the conversion factors. This is important as the detector will be permanently used as a beam monitor during all experiments.

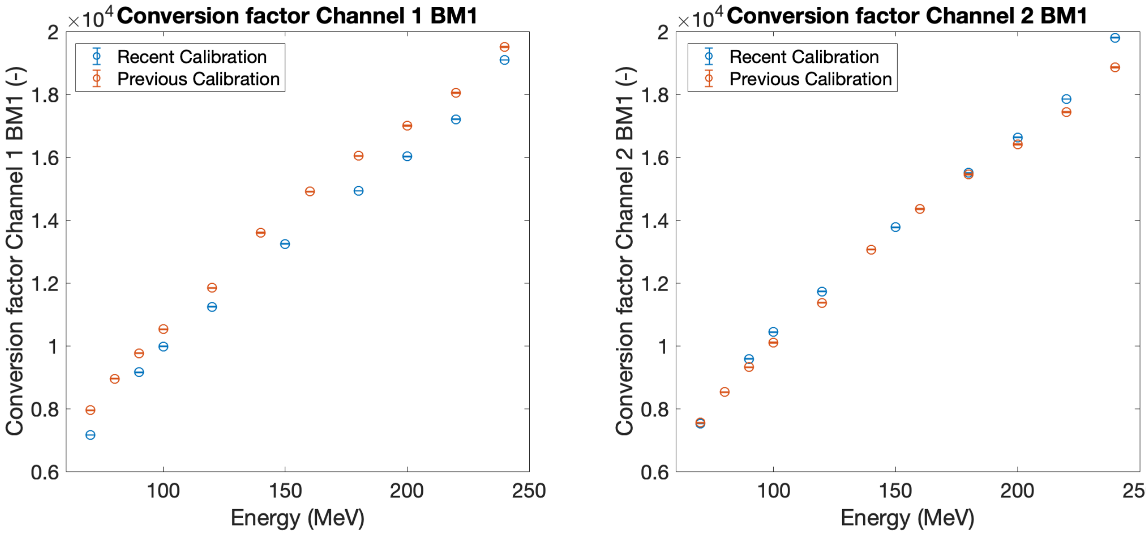

Figure 4.12: Conversion factors for integral channel 1 (left) and channel 2 (right) from the BM1 detector. Comparison between conversion factors for a previous calibration (red) and a more recent calibration (blue). On the x-axis the beam energy in MeV and on the y-axis the conversion factor.

4.4. Beam energy

4.4.1. Beam energy and Bragg peaks

The depth-dose curves measured with the Giraffe detector at the isocenter are presented in figure 4.13, with the relative dose shown as a function of depth in water. The figure shows the Bragg-peaks for nominal beam energies of 70-230 MeV. What can be seen is that the peaks are occurring deeper with increasing energy.

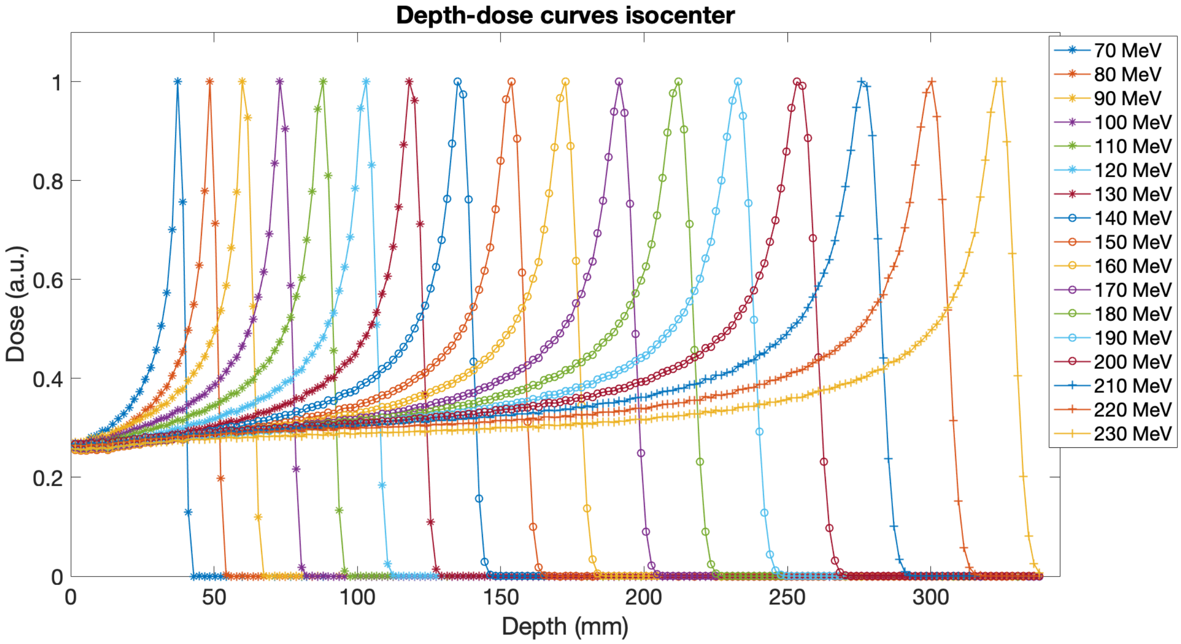

Figure 4.13: Depth-dose curves measured with the Giraffe detector at the isocenter for nominal beam energies of 70-130 MeV. On the x-axis the depth (in water) is given in mm and on the y-axis the relative dose.

The depth-dose curves have been analyzed by doing a cubic interpolation between the data points to determine the d_{80} from the raw data. It has been found that the d_{80} deduced in that way agrees with the d_{80} given by the detector software within the accuracy of 0.5 mm. The d_{80} given by the detector software is given in table 4.7. Furthermore, the beam energy at the isocenter is given, which comes from the measured d_{80}, with in the final column the uncertainty of this energy. The uncertainty is propagated from the uncertainty in d_{80}, which is ±0.5 mm. Table 4.8 shows slightly different values than table 4.7. In table 4.8 the d_{80} has been corrected for the WET of the air between the exit window and the isocenter together with the WET of the exit window itself. Determining the beam energy from this $d_{80\ corrected}$ will give the beam energy just before passing the exit window. The final column of the table gives beam energy values that have been measured in 2019 by Varian in the experimental room, which back then they also propagated back to just before the exit window. Those experiments made use of a PTW water phantom to do the Bragg peak measurements. The beam energies found previously by Varian do agree with the values found with the Giraffe detector as they fall within the uncertainty. Even though Bragg-peak measurements with a water phantom can be performed with a smaller uncertainty, measurements with an MLIC such as the Giraffe have the advantage of taking less time. Going back to the tables again the E_{ISO} in table 4.7 is always lower than the nominal energy, not taking into account the uncertainty. This makes sense as the protons are expected to have the nominal energy after the degrader and then from that point up to the target will lose energy on the way by all the material in between. $E_{Exit\ window}$ however in some cases seems to be higher than the nominal beam energy, also when not taking the uncertainty into account. This might have several reasons. First of all, it can be that it is just due to the uncertainty and the actual energy is lower than the nominal energy. Other explanations could be that the beam energy is actually higher than expected after passing the degrader material, or that the calibration of the Giraffe is not completely accurate.

Table 4.7: Proton range (d_{80}) measured with the Giraffe detector together with the resulting beam energy at the isocenter (E_{ISO}). The first column shows the nominal beam energy for which the measurement has been performed. The final column gives the uncertainty of the determined beam energy at the isocenter in MeV.

$E_{nominal}$ (MeV)	d_{80} (cm)	E_{ISO} (MeV)	$\pm u_{E\ ISO}$ (MeV)
70	3.90	68.32	0.49
80	5.02	78.64	0.44
90	6.25	88.90	0.40
100	7.57	98.99	0.37
110	9.00	109.12	0.34
120	10.52	119.18	0.32
130	12.13	129.21	0.30
140	13.84	139.29	0.29
150	15.63	149.31	0.27
160	17.51	159.37	0.26
170	19.47	169.40	0.25
180	21.49	179.34	0.24
190	23.60	189.35	0.23
200	25.78	199.34	0.23
210	28.03	209.32	0.22
220	30.37	219.39	0.21
230	32.72	229.21	0.21

4.4.2. Spread-out Bragg peaks

The Spread-out Bragg peaks have been measured for different nominal beam energies. The ridge filter used was designed for a 150 MeV proton beam. The spread-out Bragg peak for this energy is shown in figure 4.14. The figure shows the depth-dose curve measured with the Giraffe detector. In the region marked by the dashed area the plateau of the spread-out Bragg peak can clearly be seen. Figure 4.15 zooms into this region, giving a better visualization of the spread-out Bragg peak. A region of 2.8 cm is marked, and it shows that within this region there is a uniformity U of 97.9%. As the ridge filter was supposed to give a spread-out Bragg peak of at least 2.5 cm with a uniformity of 98%, it can be concluded that the ridge filter works as

Table 4.8: Proton range corrected for the WET of the air between the isocenter and exit window and the WET of the exit window ($d_{80\ corrected}$) measured with the Giraffe detector together with the resulting beam energy just before the exit window $E_{Exit\ window}$ window. The first column shows the nominal beam energy for which the measurement has been performed. The before-last column gives the uncertainty of the determined beam energy. The final column shows the beam energy determined in previous experiments done by Varian.

$E_{nominal}$ (MeV)	$d_{80\ corrected}$ (cm)	$E_{Exit\ window}$ (MeV)	$\pm u_{E\ Exit\ window}$ (MeV)	$E_{Exit\ window\ Varian}$ (MeV)
70	4.05	69.73	0.48	69.87
80	5.17	79.91	0.43	79.82
90	6.40	90.06	0.40	89,86
100	7.72	100.06	0.37	99,83
110	9.15	110.12	0.34	-
120	10.67	120.12	0.32	-
130	12.28	130.10	0.30	129.86
140	13.99	140.13	0.29	-
150	15.78	150.11	0.27	149.90
160	17.66	160.13	0.26	159.88
170	19.62	170.14	0.25	-
180	21.64	180.05	0.24	-
190	23.75	190.03	0.23	-
200	25.93	200.00	0.22	199.83
210	28.18	209.96	0.22	-
220	30.52	220.01	0.21	219.83
230	32.87	229.81	0.21	-

supposed. Other beam energies and field sizes have been investigated, to see for which other energies the ridge filter could be used. The results of the measurements are summarized in table 4.7. The table shows the uniformity of spread-out Bragg peaks of width W at different beam energies. It can be seen that up to 3.2 cm width uniformities of around 96% still can be found. For now, the 150 MeV beam energy has been the one of interest, as it is the energy for which a large uniform field will be created by means of passive scattering. To achieve a uniform field in the third dimension (depth), the ridge filter is needed and will be put in the setup in future experiments. Depending on the required uniformity and width of the spread-out Bragg peak, the ridge filter can be used for other beam energies than 150 MeV. In future experiments it can be tested for energies other than those listed in the table as well, as it shows very promising results.

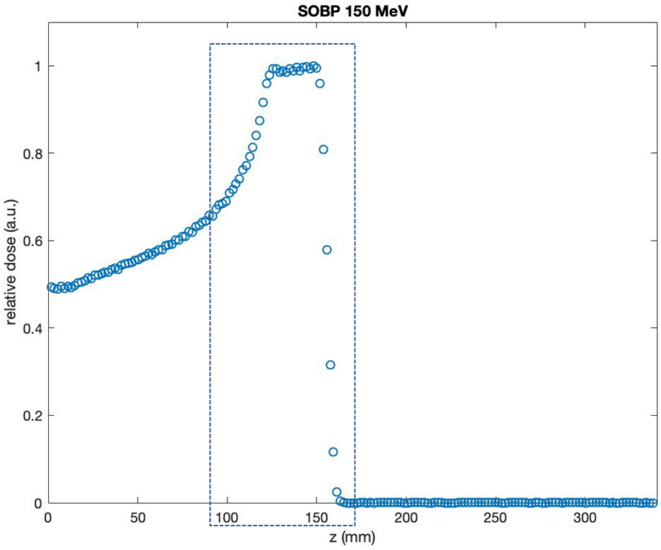

Figure 4.14: Spread-out Bragg peak measured with a nominal beam energy of 150 MeV. On the x-axis the depth z in water is given in mm and on the y-axis the relative dose. The dashed rectangular region roughly shows in which region the spread-out Bragg peak can be seen.

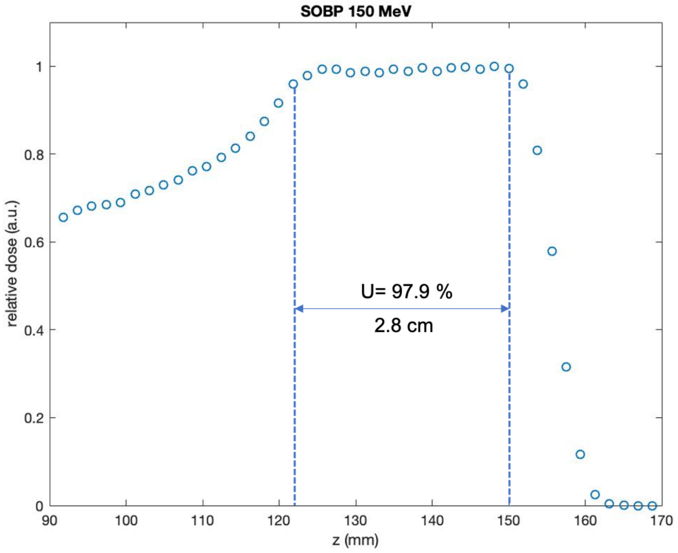

Figure 4.15: Spread-out Bragg peak measured with a nominal beam energy of 150 MeV. On the x-axis the depth z in water is given in mm and on the y-axis the relative dose. The axes are adjusted to clearly see the spread-out Bragg peak. In the graph a 2.8 cm region is marked together with the uniformity U of that region.

Table 4.9: Uniformity U for different SOBP widths W for different beam energies.

100 MeV		120 MeV		150 MeV		180 MeV		200 MeV		130 MeV	
W (cm)	U (%)	W (cm)	U (%)	W (cm)	U (%)	W (cm)	U (%)	W (cm)	U (%)	W (cm)	U (%)
3.0	96.0	3.2	95.6	3.2	95.6	3.2	95.1	3.0	95.6	3.2	95.6
2.6	98.7	2.8	98.5	2.8	97.9	2.8	97.3	2.6	97.0	2.8	97.1
2.3	98.7	2.4	98.7	2.4	98.9	2.4	98.2	2.3	98.8	2.4	98.7
1.9	98.7	2.1	98.7	2.1	99.3	2.1	99.4	1.9	99.0	2.1	99.3
1.5	99.2	1.7	99.8	1.7	99.3	1.7	99.4	1.5	99.2	1.7	99.5
1.1	99.5	1.3	99.1	1.3	99.4	1.3	99.4	1.1	99.3	1.3	99.6
0.8	99.6	0.9	99.1	0.9	99.4	0.9	99.4	0.8	99.6	0.9	99.7
0.4	99.6	0.6	99.6	0.6	99.4	0.6	99.5	0.4	99.8	0.6	99.7

4.5. Passively scattered field

The passive scattering experiments had the purpose of probing the positions between elements of the experimental setup. The beam monitor BM1 is fixed at its position of 12 cm. The positioning of the lead foil as close to the exit window as possible turned out to give the best results in terms of uniformity. The closest the foil can be placed to the exit window is at 3.5 cm. Next the position of the dual ring was found to be optimal at a distance of 45 cm from the exit window. For the positioning of the Lynx detector there are two setup possibilities:

1. Positioning the Lynx as far away as needed to get a uniform field of at least 10 cm diameter.
2. Positioning the Lynx further away to make as much use of scattering in air to obtain larger uniform fields (e.g. up to 20 cm diameter).

Both setups have an advantage and disadvantage as discussed in section 3.7.1. The positions for the Lynx that we have finally chosen are at 193 cm from the exit window for setup 1 and 281 cm for setup 2. The resulting fields are shown in figure 4.16 and figure 4.17 for setup 1 and 2 respectively. The horizontal and vertical profiles through the center of the fields are given in the same figures. In both figures the profiles have the characteristic shape as can be seen in figure 1.7 for a dual ring setup. For the second setup (figure 4.17 the profiles are flatter due to the scattering in air over a larger distance between the dual ring and the detector.

Furthermore, a small tilt is found in both of the figures when observing the profiles. Dual ring set-ups however are strongly dependant of the alignment, making it very difficult to overcome tilts becoming visible in the final field. Calculated uniformities for both of the fields are presented in table 4.10 and table 4.11. Promising results have been obtained for both setups. For the first setup fields of up to 16 cm have been found with a uniformity of at least 97%. The second setup produces fields up to 25 cm with a uniformity of again at least 97%. As the goal of the passive scattering experiments was to get a uniformity of at least 97%, it can be concluded that the experiments were successful and the distances between the beam line elements can be used for future experiments. Depending on whether a circular or square collimator is placed in the setup in the end will have an effect on the uniformity.

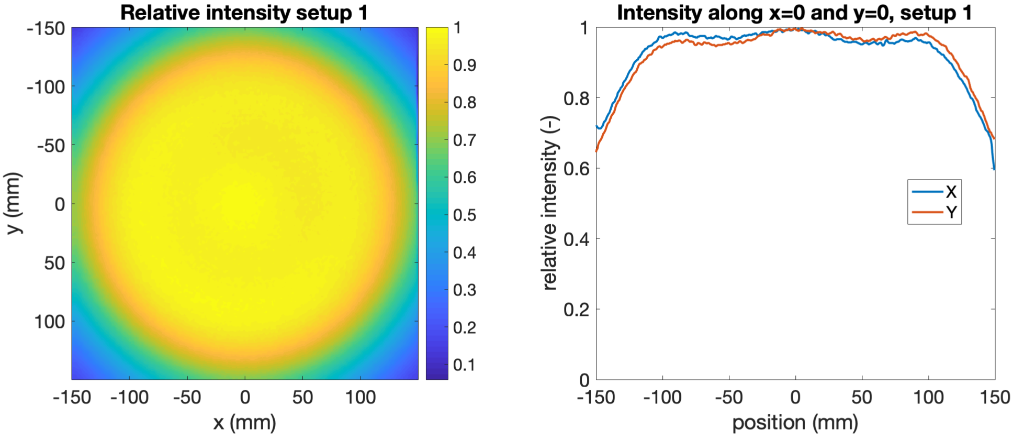

Figure 4.16: On the left the field acquired with the passive scattering setup with the Lynx positioned at 193 cm from the exit window. On the x-axis the x-position in mm and on the y-axis the y-position in mm. The colours show the relative intensity of the field. On the right the horizontal (blue) and vertical (red) profile taken from the passively scattered field. On the x-axis the position is given in mm and on the y-axis the relative intensity.

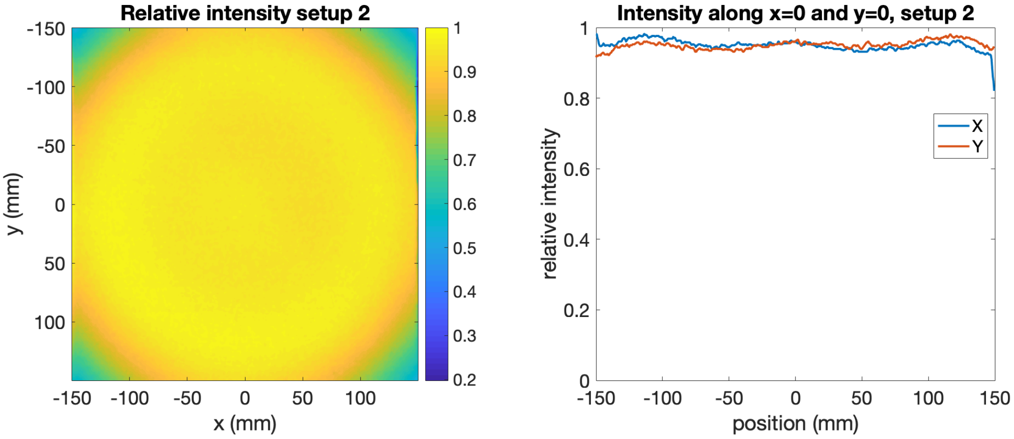

Figure 4.17: On the left the field acquired with the passive scattering setup with the Lynx positioned at 281 cm from the exit window. On the x-axis the x-position in mm and on the y-axis the y-position in mm. The colours show the relative intensity of the field. On the right the horizontal (blue) and vertical (red) profile taken from the passively scattered field. On the x-axis the position is given in mm and on the y-axis the relative intensity.

Table 4.10: Uniformity found for fields of different sizes for setup 1. U_x and U_y give the uniformities of profiles taken through the center of the field, U_{circle} the uniformity of a circular field of diameter 6, 10 or 16 cm at the center of the field and U_{square} for a square with sides of that size.

6 cm				10 cm				16 cm			
U_x (%)	U_y (%)	U_{circle} (%)	U_{square} (%)	U_x (%)	U_y (%)	U_{circle} (%)	U_{square} (%)	U_x (%)	U_y (%)	U_{circle} (%)	U_{square} (%)
98.4	98.5	97.5	98.1	97.8	97.7	97.1	97.1	97.6	97.4	95.2	97.0

Table 4.11: Uniformity found for fields of different sizes for setup 2. U_x and U_y give the uniformities of profiles taken through the center of the field, U_{circle} the uniformity of a circular field of diameter 6, 10 or 16 cm at the center of the field and U_{square} for a square with sides of that size.

16 cm				20 cm				25 cm			
U_x (%)	U_y (%)	U_{circle} (%)	U_{square} (%)	U_x (%)	U_y (%)	U_{circle} (%)	U_{square} (%)	U_x (%)	U_y (%)	U_{circle} (%)	U_{square} (%)
98.3	98.2	96.8	97.6	97.8	97.8	96.1	96.7	97.4	97.4	85.8	96.5

5

Conclusions and Future Prospects

The main goal of this thesis was to characterize the proton beam in terms of shape, current, and energy. For the beam shape the beam spot size has been characterized at the isocenter together with the asymmetry of the beam spot for nominal energies ranging from 70 to 240 MeV. Furthermore the full beam profile has been characterized in x- and y-direction with a double Gaussian and Gauss-Rutherford for a 70 MeV beam, to get a better agreement in the tails of the lateral dose distribution according to Bellinzona et al. [4]. Beam envelope measurements have been performed for five different beam energies, with the distance from the exit window varying from about 20 cm up to 2 m. Beam current measurements were done at the isocenter to determine the transmission efficiency of the system for nominal energies between 70 and 240 MeV. Knowing the transmission efficiency will allow to determine what the beam current at the isocenter will be from the nominal current. The beam current measurements also allowed us to determine calibration factors for the two integral channels of the BM1 detector. After the calibration the BM1 can be used as a beam monitor to measure the beam current and number of protons during experiments. Bragg peak measurements were performed at the isocenter. These measurements gave the depth-dose curves in water, the range of the protons, and the beam energy at the isocenter. Additionally the WET of the exit window and the air between the exit window and isocenter have been calculated, to determine the beam energy just before the exit window. The resulting energies have then be compared to values found earlier by Varian. From the characteristics that have been found it can be concluded that:

- The beam spot size at the isocenter varies from 3.66 mm for the highest beam energy up to 5.47 mm for the lowest beam energy in x-direction. In y-direction the beam spot sizes vary from 3.54 mm up to 5.29 mm.
- The asymmetry of the beam spot at the isocenter is 1.7% in the worst case.
- The beam spot size just after the exit window is about 2-3 mm and diverges up to 12 mm at 2 m from the exit window.
- The beam spot sizes at the isocenter measured during the beam envelope measurements agree with beam spot sizes measured previously with a different detector.
- The isocenter is not necessarily the position along the beam line where the beam spot is the most symmetrical. In some cases this point lies downstream of the isocenter. If a symmetric beam spot is needed for a certain experiment, this should be taken into account.
- The transmission efficiency is about 0.04% for a nominal beam energy of 70 MeV, and 5.6% for 240 MeV, increasing exponentially with increasing beam energy.
- The difference between the nominal beam energy and the beam energy at the isocenter is the biggest at a nominal beam energy of 70 MeV, and becomes smaller as the nominal beam energy goes up. The difference is 2.4% for a 70 MeV nominal beam and 0.3% for a 230 MeV nominal beam.

Furthermore the beam energies just before the exit window determined by Varian in a previous experiment fall within the uncertainty of the beam energies that have been found during this thesis. The BM1 calibration on the other hand does not agree with the previous calibration. For one of the integral channels the calibration factors do agree, but for the other channel this is not the case. As there is a difference between the channels one possible explanation could be that in the period between the two experiments work has been done on the electronics of the detector, which changed the gain of one of the channels.

The second goal of this thesis was to start the measurements with the elements meant for the passively scattered field setup. The measurements have been performed with a dual ring setup and a ridge filter, both designed for a 150 MeV proton beam. With the dual ring setup fields have been formed with a diameter up to 25 cm with uniformities of at least 97%. Two setups have been used for the double scattering with the detector placed at different distances, to be able to have a trade-off between field size and dose rate. The ridge filter was designed to create a SOBP of 2.5 cm, but for a 150 MeV beam a SOBP of even 2.8 cm has been measured with a uniformity of 98%. The ridge filter also gave good results for other beam energies.

All in all it can be concluded that the goals of the project have been reached, as the beam has been characterized in terms of shape, current, and energy. Also some preliminary work for the passive field has been accomplished by determining the optimum distances between the double scattering elements and measuring the width and uniformity of the SOBP modulated by the ridge filter. What should be noted is that all the Matlab scripts created for the data analyses can be used again in future experiments. This will drastically decrease the time needed to analyze the data, as they only need the raw data as an input and every script will then export a table with the characteristics of interest.

After finishing the project and reflecting on the results, some future recommendations are:

- Perform beam spot measurements with the Lynx detector in stead of the NextQ to decrease the uncertainty of the beam spot size.
- For a full characterization of the beam spot find a method to characterize the halo in the tails caused by nuclear interactions more accurately.
- Perform beam envelope measurements for more beam energies and if possible start closer to the exit window and finish as far as the experimental area allows (e.g. up to 3 m).
- Determine the transmission efficiency for the full range between 70 MeV and 240 MeV, as now for some beam energies the transmission efficiency is missing.
- Redo the BM1 calibration to see if the first integral channel gives different results again and perform the BM1 calibration for different nominal currents to verify whether saturation effects occur at high beam currents.

Some remaining work, not necessarily related to the beam characterization is:

- Calibrate the integral channels of the NextQ detector. The same method as for the BM1 detector can be applied. The script for the data analyses is completed already.
- Calibrate EBT3 films in terms of dose, to be able to use them in future experiments.
- Perform Bragg peak measurements with the QUBE detector to verify if the results are the same as for the experiments with the Giraffe detector.
- Determine the beam spot size at different depths in water. This would be similar to a beam envelope measurement, only measured in water instead of in air.

The work on the passively scattered field provided a setup that can be used as a base, and will be expanded by placing the ridge filter and a collimator in the setup. After completing the setup, the entire 3D field can then be characterized in terms of dose. The results obtained from the characterization of the single pencil beam allowed to start with the first physics experiments at the experimental room of HollandPTC during the last year.

A

Lynx detector settings

Table A.1: Lynx detector settings used for the beam envelope measurements.

Energy (MeV)	Distance from exit window (cm)	Nominal Current (nA)	Iris (%)	Exposure time (ms)
70	23	100	40	2500
	53	100	40	2500
	91.1	100	50	2500
	123	100	60	2500
	153	100	70	3000
	183	100	80	3000
	204.5	100	90	3000
120	23	50	30	2500
	53	50	30	2500
	91.1	50	40	2500
	123	50	40	2500
	153	50	50	3000
	183	50	60	3000
	204.5	50	70	3000
150	23	50	20	2500
	53	50	20	2500
	91.1	50	30	2500
	123	50	30	2500
	153	50	30	2500
	183	50	50	3000
	204.5	50	60	3000
200	23	10	30	2500
	53	10	30	2500
	91.1	10	40	2500
	123	10	40	2500
	153	10	50	3000
	183	10	60	3000
	204.5	10	80	3000
240	23	5	10	3000
	53	5	10	3000
	91.1	5	20	3000
	123	5	20	3000
	153	5	30	3000
	183	5	40	3000
	204.5	10	40	3000

Bibliography

[1] Ugo Amaldi. *Particle accelerators: from big bang physics to hadron THERAPY.* Springer, 2014.

[2] Louis Archambault, Jerimy C Polf, Luc Beaulieu, and Sam Beddar. Characterizing the response of miniature scintillation detectors when irradiated with proton beams. *Physics in Medicine & Biology*, 53(7): 1865, 2008.

[3] W Assmann, S Kellnberger, S Reinhardt, S Lehrack, A Edlich, PG Thirolf, M Moser, G Dollinger, M Omar, V Ntziachristos, et al. Ionoacoustic characterization of the proton bragg peak with submillimeter accuracy. *Medical physics*, 42(2):567–574, 2015.

[4] VE Bellinzona, M Ciocca, A Embriaco, A Fontana, A Mairani, M Mori, and K Parodi. On the parametrization of lateral dose profiles in proton radiation therapy. *Physica Medica*, 31(5):484–492, 2015.

[5] MJ Berger, M Inokuti, HH Andersen, H Bichsel, D Powers, SM Seltzer, D Thwaites, and DE Watt. Report 49. *Journal of the International Commission on Radiation Units and Measurements*, (2):NP–NP, 1993.

[6] Hans Bethe. Zur theorie des durchgangs schneller korpuskularstrahlen durch materie. *Annalen der Physik*, 397(3):325–400, 1930.

[7] MARIA GIUSEPPINA Bisogni, Giuseppe Antonio Pablo Cirrone, Giacomo Cuttone, Alberto Del Guerra, P Lojacono, MA Piliero, Francesco Romano, Valeria Rosso, Valeria Sipala, and Arnaldo Stefanini. Medipix2 as a tool for proton beam characterization. *Nuclear Instruments and Methods in Physics Research Section A: Accelerators, Spectrometers, Detectors and Associated Equipment*, 607(1):48–50, 2009.

[8] Thomas Bortfeld and Wolfgang Schlegel. An analytical approximation of depth-dose distributions for therapeutic proton beams. *Physics in Medicine & Biology*, 41(8):1331, 1996.

[9] Freddie Bray, Jacques Ferlay, Isabelle Soerjomataram, Rebecca L Siegel, Lindsey A Torre, and Ahmedin Jemal. Global cancer statistics 2018: Globocan estimates of incidence and mortality worldwide for 36 cancers in 185 countries. *CA: a cancer journal for clinicians*, 68(6):394–424, 2018.

[10] WT Chu, BA Ludewigt, and TR Renner. Instrumentation for treatment of cancer using proton and light-ion beams. *Review of Scientific Instruments*, 64(8):2055–2122, 1993.

[11] Julie Constanzo, Marie Vanstalle, Christian Finck, David Brasse, and Marc Rousseau. Dosimetry and characterization of a 25-mev proton beam line for preclinical radiobiology research. *Medical physics*, 46 (5):2356–2362, 2019.

[12] Marco Durante and Harald Paganetti. Nuclear physics in particle therapy: a review. *Reports on Progress in Physics*, 79(9):096702, 2016.

[13] U Fano. Penetration of protons, alpha particles, and mesons. *Annual Review of Nuclear Science*, 13(1): 1–66, 1963.

[14] JB Farr, AE Mascia, W-C Hsi, CE Allgower, F Jesseph, AN Schreuder, M Wolanski, DF Nichiporov, and V Anferov. Clinical characterization of a proton beam continuous uniform scanning system with dose layer stacking. *Medical physics*, 35(11):4945–4954, 2008.

[15] Steven J Frank and X Ronald Zhu. *Proton Therapy E-Book: Indications, Techniques, and Outcomes.* Elsevier Health Sciences, 2020.

[16] B Gottschalk, AM Koehler, RJ Schneider, JM Sisterson, and MS Wagner. Multiple coulomb scattering of 160 mev protons. *Nuclear Instruments and Methods in Physics Research Section B: Beam Interactions with Materials and Atoms*, 74(4):467–490, 1993.

[17] Virgil L Highland. Some practical remarks on multiple scattering. *Nuclear Instruments and Methods*, 129 (2):497–499, 1975.

[18] Rui-Xue Huang and Ping-Kun Zhou. Dna damage response signaling pathways and targets for radiotherapy sensitization in cancer. *Signal Transduction and Targeted Therapy*, 5(1):1–27, 2020.

[19] Yu-Mi Kim, Sang-Pil Yun, Han-Sung Kim, and Hyeok-Jung Kwon. Beam characterization of the low-flux proton beam line at komac for application to radiation effect testing. *Nuclear Instruments and Methods in Physics Research Section A: Accelerators, Spectrometers, Detectors and Associated Equipment*, 950:162971, 2020.

[20] AM Koehler, RJ Schneider, and JM Sisterson. Range modulators for protons and heavy ions. *Nuclear Instruments and Methods*, 131(3):437–440, 1975.

[21] Liyong Lin, Christopher G Ainsley, and James E McDonough. Experimental characterization of two-dimensional pencil beam scanning proton spot profiles. *Physics in Medicine & Biology*, 58(17):6193, 2013.

[22] Leonard H Luthjens, Tiantian Yao, and John M Warman. A polymer-gel eye-phantom for 3d fluorescent imaging of millimetre radiation beams. *Polymers*, 10(11):1195, 2018.

[23] Alfredo Mirandola, Giuseppe Magro, Marco Lavagno, Andrea Mairani, Silvia Molinelli, Stefania Russo, Edoardo Mastella, Alessandro Vai, Davide Maestri, Vanessa La Rosa, et al. Characterization of a multi-layer ionization chamber prototype for fast verification of relative depth ionization curves and spread-out-bragg-peaks in light ion beam therapy. *Medical physics*, 45(5):2266–2277, 2018.

[24] Gert Moliere. Theorie der streuung schneller geladener teilchen i. einzelstreuung am abgeschirmten coulomb-feld. *Zeitschrift für Naturforschung A*, 2(3):133–145, 1947.

[25] Gert Moliere. Theorie der streuung schneller geladener teilchen ii mehrfach-und vielfachstreuung. *Zeitschrift für Naturforschung A*, 3(2):78–97, 1948.

[26] Konrad Pawel Nesteruk, Martin Auger, Saverio Braccini, Tommaso Stefano Carzaniga, Antonio Ereditato, and Paola Scampoli. A system for online beam emittance measurements and proton beam characterization. *Journal of instrumentation*, 13(01):P01011, 2018.

[27] Wayne D Newhauser and Rui Zhang. The physics of proton therapy. *Physics in Medicine & Biology*, 60 (8):R155, 2015.

[28] NIST. Stopping-power and range tables for protons, May 2020. URL `https://physics.nist.gov/PhysRefData/Star/Text/PSTAR.html`.

[29] Harald Paganetti. *Proton therapy physics*. CRC press, 2018.

[30] Sae-Hoon Park and Yu-Seok Kim. Characterization of the beam profile for the pixe/pige beam line at the crc proton cyclotron. *Journal of the Korean Physical Society*, 63(7):1291–1295, 2013.

[31] E Pedroni, S Scheib, T Böhringer, A Coray, M Grossmann, S Lin, and A Lomax. Experimental characterization and physical modelling of the dose distribution of scanned proton pencil beams. *Physics in Medicine & Biology*, 50(3):541, 2005.

[32] M Piccinini, C Ronsivalle, A Ampollini, G Bazzano, L Picardi, P Nenzi, E Trinca, M Vadrucci, F Bonfigli, E Nichelatti, et al. Proton beam spatial distribution and bragg peak imaging by photoluminescence of color centers in lithium fluoride crystals at the top-implart linear accelerator. *Nuclear Instruments and Methods in Physics Research Section A: Accelerators, Spectrometers, Detectors and Associated Equipment*, 872:41–51, 2017.

[33] G Polge, L Dusseau, K Idri, D Plattard, JR Vaille, G Ranchoux, J Fesquet, J Gasiot, and N Iborra-Brassard. Characterization of a 63 mev proton beam with optically stimulated luminescent films. In *RADECS 2001. 2001 6th European Conference on Radiation and Its Effects on Components and Systems (Cat. No. 01TH8605)*, pages 1–5. IEEE, 2001.

[34] MDH Rituerto Prieto. Passive Beam Field Characterization for Application in Radiobiology. Master's thesis, Delft University of Technology, the Netherlands, 2020.

[35] PTCOG. Particle therapy facilities in clinical operation (last update: Sep 2020), November 2020. URL `https://www.ptcog.ch/index.php/facilities-in-operation`.

[36] Gabriel O Sawakuchi, X Ronald Zhu, Falk Poenisch, Kazumichi Suzuki, George Ciangaru, Uwe Titt, Aman Anand, Radhe Mohan, Michael T Gillin, and Narayan Sahoo. Experimental characterization of the low-dose envelope of spot scanning proton beams. *Physics in Medicine & Biology*, 55(12):3467, 2010.

[37] Dieter Schardt, Thilo Elsässer, and Daniela Schulz-Ertner. Heavy-ion tumor therapy: Physical and radiobiological benefits. *Reviews of modern physics*, 82(1):383, 2010.

[38] J Schwaab, Stephan Brons, J Fieres, and Katia Parodi. Experimental characterization of lateral profiles of scanned proton and carbon ion pencil beams for improved beam models in ion therapy treatment planning. *Physics in Medicine & Biology*, 56(24):7813, 2011.

[39] Yuri Simeonov, Uli Weber, Petar Penchev, Toke Printz Ringbæk, Christoph Schuy, Stephan Brons, Rita Engenhart-Cabillic, Jens Bliedtner, and Klemens Zink. 3d range-modulator for scanned particle therapy: development, monte carlo simulations and experimental evaluation. *Physics in Medicine & Biology*, 62 (17):7075, 2017.

[40] Frédéric Stichelbaut and Yves Jongen. Properties of an energy degrader for light ions. *Progress in Nuclear Science and Technology*, 4:272–275, 2014.

[41] Yoshihisa Takada. Dual-ring double scattering method for proton beam spreading. *Japanese journal of applied physics*, 33(1R):353, 1994.

[42] F Tommasino, M Rovituso, S Fabiano, S Piffer, C Manea, S Lorentini, S Lanzone, Z Wang, M Pasini, WJ Burger, et al. Proton beam characterization in the experimental room of the trento proton therapy facility. *Nuclear Instruments and Methods in Physics Research Section A: Accelerators, Spectrometers, Detectors and Associated Equipment*, 869:15–20, 2017.

[43] Francesco Tommasino, Marta Rovituso, Eleonora Bortoli, Chiara La Tessa, Giada Petringa, Stefano Lorentini, Enrico Verroi, Yuri Simeonov, Ulrich Weber, Pablo Cirrone, et al. A new facility for proton radiobiology at the trento proton therapy centre: Design and implementation. *Physica Medica*, 58:99–106, 2019.

[44] L Torrisi. Plastic scintillator investigations for relative dosimetry in proton-therapy. *Nuclear Instruments and Methods in Physics Research Section B: Beam Interactions with Materials and Atoms*, 170(3-4):523–530, 2000.

[45] Linh T Tran, Lachlan Chartier, David Bolst, Alex Pogossov, Susanna Guatelli, Marco Petasecca, Michael LF Lerch, Dale A Prokopovich, Mark I Reinhard, Benjamin Clasie, et al. Characterization of proton pencil beam scanning and passive beam using a high spatial resolution solid-state microdosimeter. *Medical physics*, 44(11):6085–6095, 2017.

[46] KWA van Dongen, AJ de Blécourt, E Lens, DR Schaart, and FM Vos. Reconstructing 3d proton dose distribution using ionoacoustics. *Physics in Medicine & Biology*, 64(22):225005, 2019.

[47] JM Warman, MP De Haas, LH Luthjens, AG Denkova, O Kavatsyuk, M-J Van Goethem, HH Kiewiet, and S Brandenburg. Fixed fluorescent images of an 80 mev proton pencil beam. *Radiation Physics and Chemistry*, 85:179–181, 2013.

[48] WHO. Cancer, November 2020. URL `https://www.who.int/news-room/fact-sheets/detail/cancer`.

[49] Robert R Wilson. Radiological use of fast protons. *Radiology*, 47(5):487–491, 1946.

[50] Rui Zhang and Wayne D Newhauser. Calculation of water equivalent thickness of materials of arbitrary density, elemental composition and thickness in proton beam irradiation. *Physics in Medicine & Biology*, 54(6):1383, 2009.